Department of Applied Physics

Optical Properties of Single-walled Carbon Nanotubes and Nanobuds

Ying Tian

Aalto University

DOCTORAL DISSERTATIONS

Aalto University publication series
DOCTORAL DISSERTATIONS 77/2012

Optical Properties of Single-walled Carbon Nanotubes and Nanobuds

Ying Tian

Doctoral dissertation for the degree of Doctor of Science in Technology (Doctor of Philosophy) to be presented with due permission of the School of Science for public examination and debate in Auditorium F of the main building at the Aalto University School of Science (Espoo, Finland) on the 8th of June 2012 at 13 o'clock.

Aalto University
School of Science
Department of Applied Physics
NanoMaterials Group

Supervisor
Prof. Esko I. Kauppinen

Instructor
Dr. Albert G. Nasibulin

Preliminary examiners
Prof. Daniel E.Resasco, University of Oklahoma, USA
Prof. Homma Toshikazu, Tokyo University of Science, Japan

Opponent
Prof. Saito Riichiro, Tohoku University, Japan

Aalto University publication series
DOCTORAL DISSERTATIONS 77/2012

ISBN 978-952-60-4659-4 (printed)
ISBN 978-952-60-4660-0 (pdf)
ISSN-L 1799-4934
ISSN 1799-4934 (printed)
ISSN 1799-4942 (pdf)

Unigrafia Oy
Helsinki 2012

Finland

The dissertation can be read at http://lib.tkk.fi/Diss/

441 697
Printed matter

Author
Ying Tian

Name of the doctoral dissertation
Optical properties of single-walled carbon nanotubes and nanobuds

Publisher School of Science

Unit Department of Applied Physics

Series Aalto University publication series DOCTORAL DISSERTATIONS 77/2012

Field of research Nanomaterials, physics

Manuscript submitted 12 March 2012 **Manuscript revised** 7 May 2012

Date of the defence 8 June 2012 **Language** English

☐ **Monograph** ☒ **Article dissertation (summary + original articles)**

Abstract

This thesis presents the study of the optical properties of single-walled carbon nanotubes (SWCNTs) and carbon nanobuds by means of optical spectroscopy and electron microscopy. A novel analysis method that is based on optical absorption spectroscopy was developed in order to meet the challenge of accurately and efficiently evaluating the diameter distribution in any bulk SWCNT sample. Properties of SWCNTs that were synthesized both in lab-scale and semi-industrial scale aerosol reactors were investigated in detail by using the proposed method. The results show that the diameter of SWCNTs can be easily altered over a broad range from 1.1 to 1.9 nm in the same reactor by varying the growth conditions. This opens up a new route towards diameter control in the synthesis of SWCNTs. The further application, that of SWCNTs with optimized properties deposited as thin films on a saturable absorber, was also demonstrated in this work.

The other important work in this thesis involves the optical properties of carbon nanobuds. Focusing on a freestanding individual nanobud, as opposed to bulk samples of nanobuds, allowed us for the first time to observe the Raman features of a nanobud with Raman spectroscopy. The simultaneous presence of SWCNT and fullerene features in the Raman spectrum is in good agreement with independent TEM and ED investigations of the same nanobud structure, which confirmed the Raman measurement interpretation of the SWCNT chirality assignment (16,11), as well as the presence of fullerenes on the surface of the SWCNT.

Keywords SWCNT, nanobud, optical property, synthesis, diameter

ISBN (printed) 978-952-60-4659-4 **ISBN (pdf)** 978-952-60-4660-0

ISSN-L 1799-4934 **ISSN (printed)** 1799-4934 **ISSN (pdf)** 1799-4942

Location of publisher Espoo **Location of printing** Helsinki **Year** 2012

Pages 105 **The dissertation can be read at** http://lib.tkk.fi/Diss/

Acknowledgements

The research work presented in this thesis was carried out in the Nanomaterials Group of the Department of Applied Physics at the Aalto University School of Science (known as the Helsinki University of Technology before 2011).

I feel very lucky to have had the chance to study as part of Prof. Esko I. Kauppinen's group, and am very happy that he accepted me as a research student. Prof. Kauppinen has been a mentor and has taught me many things, not only in the field of science, but also in life. The experience working in his group will benefit me for the rest of my life.

I am forever indebted to my co-supervisor, Dr. Albert G. Nasibulin, for his valuable scientific advice, unceasing support, and for providing a creative and relaxed working atmosphere. It is a very joyful experience to work with you!

I owe special thanks to Dr. Hua Jiang for the personal help and the continuous support with the excellent transmission electron microscopy work in all my publications. Without you, many important optical results would not be so well certified.

Thank you to all my co-authors for their input into this thesis, especially, Dr. Jan v. Pfaler, Dr. Samuli Kivistö, Dr. Brad Aitchison, Dr. Paola Ayala, Timur Nikitin, Dr. David P. Brown, Dr. Leonid Khriachtchev, Prof. Abdou Hassanien, and Prof. Oleg G. Okhotnikov.

I wish to acknowledge all my colleagues from the Nanomaterials Group, thank you for welcoming me from the beginning and for making me feel as member of the big family. In particular, Anton S. Anisimov, Prasantha Mudimela, Delphine Chassaing, Marina Timmermans, Larisa Nasibulina, Zhu Zhen, Toma Susi, Kimmo Mustonen, Ilya Anoshkin, Simas Rackauskas and Antti Kaskela.

Furthermore, I would like to thank the pre-examiners of the thesis Prof. Daniel E. Resasco and Prof. Homma Toshikazu.

Finally, I am deeply appreciative of my family members and my friends both in Finland and in China for their eternal love and encouragement. My little boy Dawei also deserves a "thanks" for speeding up the writing process. I love you all so much!

Contents

Acknowledgements ..... **I**

Contents ..... **II**

Thesis Publications ..... **III**

Author's Contribution ..... **IV**

Other Featured Publications ..... **V**

List of Symbols and Abbreviations ..... **VI**

1. Introduction **1**

2. Carbon Nanotubes - Structure and Optical Properties **3**

2.1 Geometry of SWCNTs 3

2.2 Electronic Structure of SWCNTs 5

2.3 Optical Properties of SWCNTs 7

2.3.1 Optical Absorption Spectroscopy 7

2.3.2 Resonant Raman Spectroscopy 11

3. Experimental **16**

3.1 Synthesis Method and Techniques 16

3.1.1 Lab-scale Aerosol Reactor 16

3.1.2 Semi-industrial Scale Aerosol Reactor 18

3.1.3 Absorber Fabrication and Laser Experimental Setup 18

3.2 Characterizations 19

3.2.1 Electron Microscopy 19

3.2.2 Optical Spectroscopy 20

4. Results and Discussion **21**

4.1 Local Study of a Nanobud Structure 21

4.2 Analysis Method for Size Distribution of SWCNTs based on Absorption Spectra 25

4.3 Synthesis and Properties of SWCNTs 31

4.3.1 Lab-scale aerosol reactor 31

4.3.2 Semi-industrial Scale Aerosol Reactor 40

4.4 Optical Application of SWCNTs as Saturation Absorber 44

5. Conclusions **47**

6. References **49**

Appendices

Publications I–V

Thesis Publications

I. **Tian, Y.,** Chassaing, D., Nasibulin, A. G., Ayala, P., Jiang, H., Anisimov, A. S., and Kauppinen, E. I., Combined Raman Spectroscopy and Transmission Electron Microscopy Studies of a NanoBud Structure, Journal of American Chemical Society 130, 7188-7189 (2008).

II. **Tian, Y.**, Jiang, H., Pfaler, J., Zhu, Zh., Nasibulin A., G., Nikitin, T., Aitchison, B., Khriachtchev, L., Brown, D. P., and Kauppinen, E. I., Analysis of the Size Distribution of Single-Walled Carbon Nanotubes Using Optical Absorption Spectroscopy, Journal of Physical Chemistry Letters 1, 1143-1148 (2010).

III. **Tian, Y.,** Timmermans, M. Y., Partanen, M., Nasibulin, A. G., Jiang, H., Zhu, Z., Kauppinen, E. I., Growth of single-walled carbon nanotubes with controlled diameters and lengths by an aerosol method, Carbon 49, 4636-4643 (2011).

IV. **Tian, Y.,** Zavodchikova, M. Kivistö, S., Nasibulin, A. G., Zhu, Z., Jiang, H., Okhotnikov, O. G., and Kauppinen, E. I., Tailoring the Diameters of Single-walled Carbon Nanotubes for Optical Applications, Nano Research 4, 807-815 (2011).

V. **Tian, Y.,** Nasibulin, A. G., Aitchison, B., Nikitin, T., Pfaler, J., Jiang, H., Zhu, Zh., Khriachtchev, L., Brown, D. P., and Kauppinen, E I., Controlled Synthesis of Single-walled Carbon Nanotubes in an Aerosol Reactor, Journal of Physical Chemistry C 115, 7309-7318 (2011).

Author's Contribution

I. The author is mainly responsible for the work (apart from the TEM measurements) and wrote the manuscript.

II. The author is mainly responsible for the work (apart from TEM measurements and Matlab coding) and wrote the manuscript.

III. The author is responsible for optical absorption, Raman and PL measurements, data analysis, part of the sample preparation, and wrote the manuscript.

IV. The author is responsible for the optical measurements, data analysis and wrote the manuscript.

V. The author is mainly responsible for the work (apart from TEM measurements) and wrote the manuscript.

Other Featured Publications

I. **Tian, Y**., Chassaing, D., Nasibulin, A.G., Ayala, P., Jiang, H., Anisimov, A.S., Hassanien, A., and Kauppinen, E.I., The local study of a nanobud structure, Physica Status Solidi B 245, 2047-2050 (2008).

II. Sun, D., Timmermans, M.Y., **Tian, Y**., Nasibulin, A.G., Kauppinen, E.I., Kishimoto, S., Mizutani, T., and Ohno, Y., Flexible high-performance carbon nanotube integrated circuits, Nature Nanotechnology 6, 156-161 (2011).

III. Yu, B., Liu, Ch., Hou, P.X., **Tian, Y.,** Li, S.S., Liu,B.L., Li, F., Kauppinen, E.I., and Cheng, H.M., Bulk Synthesis of Large Diameter Semiconducting Single-Walled Carbon Nanotubes by Oxygen-Assisted Floating Catalyst Chemical Vapor Deposition, Journal of American Chemical Society 133, 5232-5235 (2011).

IV. He, M., Rikkinen, E., Zhu, Z., **Tian, Y.,** Anisimov, A.S., Jiang, H., Nasibulin, A.G., Kauppinen, E.I., Niemelä, M., Krause, O.I., Temperature Dependent Raman Spectra of Carbon Nanobuds, Journal of Physical Chemistry C 114, 13540-13545 (2010).

V. Kaskela, A., Nasibulin, A.G., Zavodchikova, M., Aitchison, B., Papadimitratos, A., **Tian, Y.,** Zhu, Z., Jiang, H., Brown, D.P., Zakhidov, A., and Kauppinen, E.I., Aerosol synthesized SWCNT networks with tuneable conductivity and transparency by dry transfer technique, Nano Letters 10, 4349-4355 (2010).

VI. Susi, T., Kaskela, A., Zhu, Z., Ayala, P., Arenal, R., **Tian, Y.,** Laiho, P., Mali, J., Nasibulin, A.G., Jiang, H., Lanzani, G., Stephan, O., Laasonen, K., Pichler, T., Loiseau, A., and Kauppinen, E.I., Nitrogen-Doped Single-Walled Carbon Nanotube Thin Films Exhibiting Anomalous Sheet Resistances, Chemistry of Materials 23, 2201-2208 (2011).

List of Symbols and Abbreviations

1D	one-dimensional
2D	two-dimensional
3D	three-dimensional
BWF	Breit-Wigner-Fano
CNT	carbon nanotube
CVD	chemical vapour deposition
CO	carbon monoxide
CO_2	carbon dioxide
cm^{-1}	wavenumber
DOS	density of states
DFT	density-functional theory
d_t	diameter
ED	electron diffraction
eV	electron volt
ESP	electrostatic precipitator
E_{SF}	electron self-energy
E_{EXB}	exciton binding energy
ETB	extended tight binding
FE	Fermi energy
HRTEM	high-resolution transmission electron microscope
H_2O	water
IS	semi-industrial scale
LS	lab-scale
MB	many-body
M	metallic
nm	nanometer
OAS	optical absorption spectroscopy
PL	photoluminescence
RBM	radial breathing mode
SWCNT	single-walled carbon nanotube
S	semiconducting
SEM	scanning electron microscope
STM	scanning tunnelling microscope
SAM	saturable absorber mirror
UV-Vis-NIR	ultraviolet-visible-near infrared
vHs	van Hove singularity

1. Introduction

Carbon nanotubes (CNTs), and in particular single-walled carbon nanotubes (SWCNTs), have attracted great interest due to their unique electronic, optical, thermal and mechanical properties that make them useful for various applications [1]The most common synthesis methods are arc-discharge, laser desorption, and chemical vapour deposition (CVD). Arc-discharge and laser ablation methods involve the vaporization of solid carbon targets. The advantage of these methods is the high crystallinity of the resultant CNT sample. However, these methods require a large energy input to evaporate graphite, and therefore it is difficult to control the growth conditions. In addition, the final products consist of a complex mixture of carbonaceous materials and catalysts, making purification a necessary process step [1, 2]. The CVD method on the other hand has been found to be efficient and selective for the growth of either SWCNTs or multiwalled carbon nanotubes. The aerosol (floating catalyst CVD) synthesis method [3-7] in particular has potential as regards large scale SWCNT production, since it is a continuous process that involves both catalyst particle formation and SWCNT growth. In addition, as this approach allows for direct sampling of SWCNTs from the gaseous phase by filtering and subsequent transferring onto practically any substrate at room temperature, there is another practical advantage over other methods [8]. The SWCNT samples studied in this thesis were synthesized by using the aerosol method.

The structure (diameter and chiral angle) of a SWCNT can fully determine whether the nanotube is either metallic or semiconducting with varying band gaps. It is thus crucial to be able to produce SWCNTs with selective properties, in order to fit the requirements called for in specific applications. Although scientists have been in pursuit of the controlled synthesis of SWCNTs with only a single diameter and chiral angle for more than two decades, it is still not possible to grow or sort a specific single nanotube structure. All production and sorting procedures end up with a mixture of SWCNTs with different diameters and chiral angles. For practical applications, the first step to improved selectivity during the SWCNT production process involves information feedback coming from a reliable characterization of the mean diameter and the diameter distribution in the raw SWCNT material that has been produced.

Motivated in this context, in this thesis, we intended to solve the above-mentioned problems. Firstly, a novel method for effective assignment of diameter distributions of a bulk SWCNT sample was successfully developed, using the optical absorption spectrum (OAS) of the sample. Compared with

the canonical approach, this method can be used as a versatile tool to analyze absorption spectra, regardless of the form or overlap of the absorption bands. Furthermore, by the means of optical measurements in combination with electron microscopy, the properties of SWCNTs and related growth mechanisms were investigated in detail as functions of various parameters in two different aerosol reactors. The mean diameter of SWCNTs can be easily controlled in a broad range from between 1.1 to 1.9 nm by altering the synthesis conditions in the same reactor. This selective growth of SWCNTs with a wide range of diameter modulation provides an opportunity to tune the electronic structure of SWCNTs to suit specific applications. For example, the sub-picosecond operations of mode-locked fiber lasers at ~1.56 μm and ~2 μm have shown improvements in their performance after the optimization of SWCNT properties.

The other important work in this thesis consists of a local study on an individual nanobud in which the fullerenes are covalently bonded to the outer surface of the SWCNT. Focusing on the single freestanding nanobud structure allowed us to observe for the first time the characteristic features of both SWCNT and fullerenes in the Raman spectrum. The atomic structure of the same nanobud was studied independently using high-resolution transmission electron microscopy (HRTEM) and electron diffraction (ED).

The thesis is organised as follows: after the introduction of the main work in chapter 1, fundamental concepts and some of the physical and optical properties of SWCNTs are presented in chapter 2. This will provide the foundation upon which the results that are presented later will be based. The experiments and characterization methods are described in chapter 3, which will be referenced throughout this work. Chapter 4 presents the results of the research conducted during the PhD study. In that chapter, the local study of a nanobud is introduced first, based on Paper I. Then, the development of a novel method of characterization based on OAS is described, with the details supported by Paper II. This universal method is used to evaluate the mean diameter and the diameter distribution of SWCNTs that are synthesized in two different aerosol reactors. Both the properties of SWCNTs and their related growth mechanisms are investigated, based on Paper III and V. Additional applications of SWCNT thin films as saturable absorber are considered (Paper IV). Finally, the conclusions of this thesis are drawn in Chapter 5.

2. Carbon Nanotubes - Structure and Optical Properties

Carbon nanotubes are long hollow cylindrical nanostructures comprised solely of carbon atoms. Most of the fascination with this material, and many of its unique properties, stems from its unusual structure and aspect ratio. The cylinder is made up of a single layer of sp^2-bonded carbon, with a diameter of a few nanometers, and a typical length of several micrometers. Both single-walled and multiwalled forms of this material exist, but the physical properties of SWCNTs have proved to be much more interesting, and it is these that will be addressed in the following chapter. They can be considered as quasi one-dimensional (1D) systems, and exhibit unusual electrical and mechanical properties.

2.1 Geometry of SWCNTs

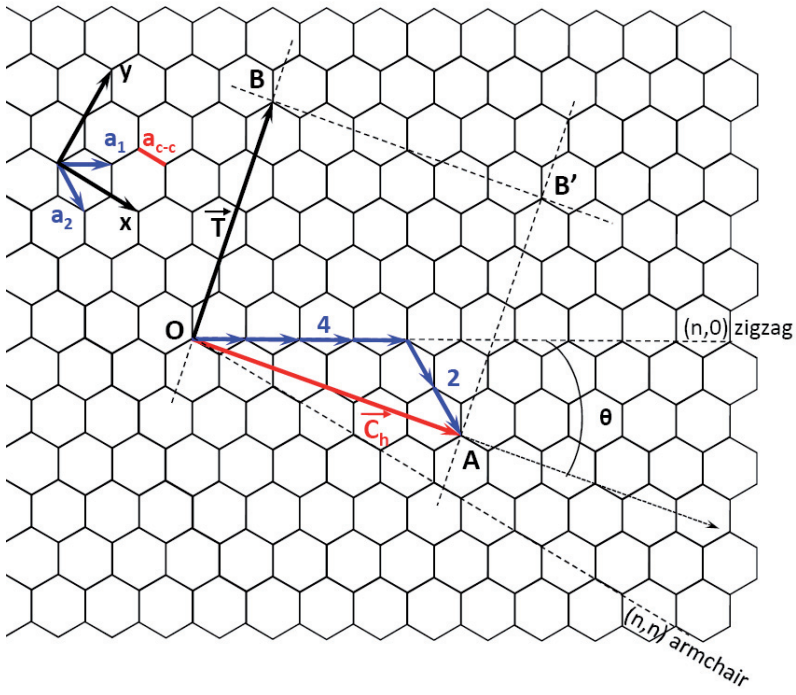

Figure 2.1 The unrolled honeycomb lattice of a nanotube. The $\overrightarrow{OA}$ and $\overrightarrow{OB}$ define the chiral vector $\vec{C}_h$ and the translation vector $\vec{T}$ of the nanotube, respectively. The figure corresponds to a chiral vector $\vec{C}_h$ = (4, 2) SWCNT. The chiral angle is indicated by θ.

A SWCNT is constructed by rolling a two dimensional (2D) graphene sheet into a narrow cylinder (graphite is a layered 3D material, and a single layer of graphite is called 2D graphite, or a graphene layer). In Fig. 2.1, the unrolled honeycomb lattice of the nanotube is shown, in which $\overrightarrow{OB}$ is the direction of the nanotube axis, and the direction of $\overrightarrow{OA}$ corresponds to the equator [9]. By rolling the honeycomb sheet so that points O and A coincide, a carbon nanotube can be constructed. The chiral vector $\vec{C}_h$ fully determines the geometry of a SWCNT, and is expressed in terms of the real space unit vectors $\vec{a}_1$ and $\vec{a}_2$ of the hexagonal lattice:

$$\vec{C}_h = n\vec{a}_1 + m\vec{a}_2 \equiv (n,m)\,,\ (n,m \text{ are positive integers}, n \geq m) \qquad (2.1)$$

In Cartesian coordinates, the unit vectors $\vec{a}_1$ and $\vec{a}_1$ can be expressed as:

$$\vec{a}_1 = \left(\frac{\sqrt{3}}{2}a, \frac{a}{2}\right), \quad \vec{a}_2 = \left(\frac{\sqrt{3}}{2}a, -\frac{a}{2}\right), \qquad (2.2)$$

where $|\vec{a}_1| = |\vec{a}_2| = a = \sqrt{3}a_{cc}$, and $a_{cc} = 1.42$ Å is the distance between neighbouring carbon atoms. The diameter of the SWCNT is given by $d_t = |\vec{C}_h| = a\sqrt{n^2 + m^2 + nm}.$ The angle θ that $\vec{C}_h$ makes with $\vec{a}_1$ is called the chiral angle, and from symmetry arguments $0 \leq \theta \leq 30^\circ$. The chiral angle θ can be defined by an expression involving $\cos(\theta)$:

$$\cos\theta = \frac{\vec{C}_h \bullet \vec{a}_1}{|\vec{C}_h||\vec{a}_1|} = \frac{2n+m}{2\sqrt{n^2+m^2+nm}}. \qquad (2.3)$$

Thus θ is related to the integers (n, m), defined in Eq.(2.1). If m=0, then $\theta = \cos^{-1}(1) = 0$, and the nanotubes are called 'zigzag' (n, 0) nanotubes, and if n=m, then $\theta = \cos^{-1}(\sqrt{3}/2) = 30°$, in this case the nanotubes are of the 'armchair' (n, n) variety. Otherwise, they are referred to as chiral (n, m) nanotubes.

The translation vector $\vec{T}$ is parallel to the nanotube axis and is normal to the chiral vector $\vec{C}_h$ in the unrolled lattice, as shown in Fig. 2.1. The lattice vector is defined as $\vec{T} = t_1\vec{a}_1 + t_2\vec{a}_2 \equiv (t_1, t_2)$, where

$$t_1 = \frac{2m+n}{d_R}, \quad t_2 = \frac{2n+m}{d_R}. \qquad (2.4)$$

The value d_R in equation (2.4) is the greatest common divisor (gcd) of (2m+n) and (2n+m). By introducing d as the greatest common divisor of n and m, d_R can be related to d by

$$d_R = \begin{cases} d & \text{if } n-m \text{ is not a multiple of } 3d \\ 3d & \text{if } n-m \text{ is a multiple of } 3d \end{cases} . \qquad (2.5)$$

The vectors $\vec{C}_h$ and $\vec{T}$ define the rectangle OAB'B in Fig. 2.1, which encloses the unit cell of the SWCNT. The number of hexagons in the unit cell is N, where

$$N = \frac{\left|\vec{C}_h \times \vec{T}\right|}{\left|\vec{a}_1 \times \vec{a}_2\right|} = \frac{2(m^2 + n^2 + nm)}{d_R} . \qquad (2.6)$$

We note that each hexagon contains two carbon atoms. Thus there are 2N carbon atoms in each unit cell of such carbon nanotubes.

2.2 Electronic Structure of SWCNTs

The electronic structure of SWCNTs is derived via a simple tight-binding (TB) calculation for the π-electrons of carbon atoms, which are the most important electrons for determining the solid-state properties of the material. Since many physical properties of SWCNTs are very similar to those of other carbon systems, particularly graphite/grapheme [10], it is often convenient to begin with the well-known properties of graphite, and then consider them in the 1D geometry of a SWCNT. The energy dispersion relations for 2D graphite are shown in Fig. 2.2.

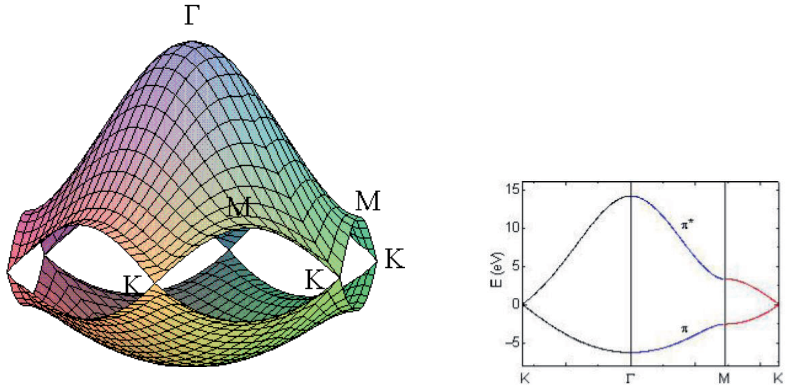

Figure 2.2 The energy dispersion relations for 2D graphite are shown throughout the whole region of the Brillouin zone. The labels indicate the high symmetry points. The right figure shows the energy dispersion along the high symmetry directions of the triangle ΓMK shown in Fig. 2.3. Adapted with permission from [11], copyright 2000 by The American Physical Society.

We can now consider the periodic boundary conditions that result from wrapping the graphene sheet into a tubular structure. The electron wave vector associated with the translation vector $\vec{T}$ (along the nanotube axis) remains continuous for a nanotube of infinite length, while the wave vector along the nanotube circumferential direction, denoted by chirality vector $\vec{C}_h$, becomes quantized. The remaining allowed wave vectors can be represented as a set of lines in the dispersion relation of graphene (Fig. 2.3). When the energy dispersion relation of graphene is denoted by E_{g2D}, the N pairs of the 1D energy dispersion relations of a SWCNT are given by

$$E_\mu(k) = E_{g2D}(k\frac{K_2}{|K_2|} + \mu K_1), \quad \left(\mu = 1,\ldots,N, and -\frac{\pi}{T} < k < \frac{\pi}{T}\right). \qquad (2.7)$$

Here, k denotes the wave number along the SWCNT axis, and the cuts are made on the lines of $kK_2/|K_2| + \mu K_1$. The energy dispersion curves described by Eq. 2.7 correspond to the cross sections of the 2D energy dispersion surface shown in Fig. 2.2.

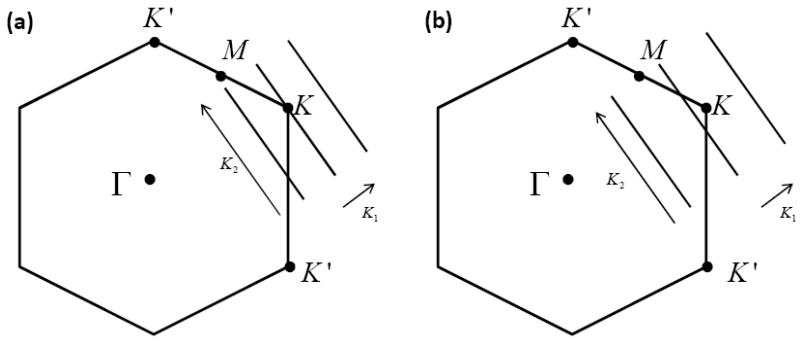

Figure 2.3 The wave vector k for 1D SWCNTs is represented in the 2D Brillouin zone of graphite (hexagon) as bold lines for (a) metallic and (b) semiconducting SWCNT. (a) For metallic nanotubes, the bold line (allowed state) intersects a K point at the Fermi energy of graphite. (b) For semiconducting nanotubes, the bold line does not go through a K point, with a finite energy band gap. Adapted with permission from [11], copyright 2000 by The American Physical Society.

If for a particular (n, m) nanotube, the cutting line passes through a K point of the 2D Brillouin zone (Fig. 2.3 (a)), where the π and π * energy bands of 2D graphite are degenerate due to symmetry, and the 1D energy bands have a zero-energy gap, and therefore they are metallic (M) carbon nanotubes. If, however, the cutting line does not pass through a K point, then the SWCNT exhibits semiconducting (S) behaviour, with a finite energy gap between the valence and conduction bands (see Fig. 2.3 (b)).

From these geometrical arguments it can be derived that SWCNTs with indices (n, m) where mod (n-m, 3) =0 are metallic, whereas SWCNTs for which mod (n-m, 3)≠0 are semiconducting. Since the SWCNT is a 1D system, the electronic density of states (DOS) vs. energy presents the characteristic van Hove singularities (vHs). Fig.2.4 shows examples of the calculated density of states (DOS) for (4, 2) semiconducting and (5, 5) metallic SWCNTs.

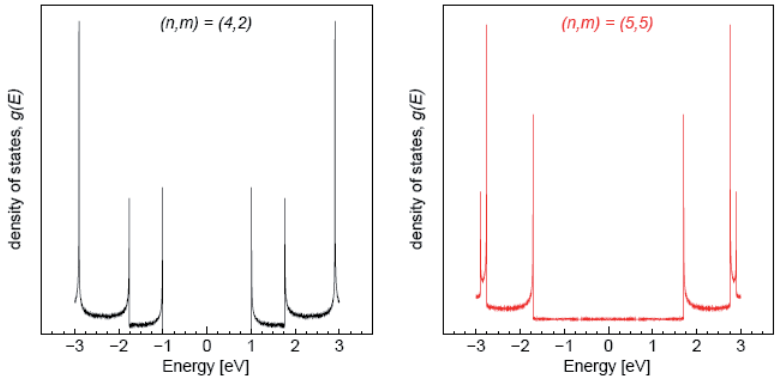

Figure 2.4. Plots of the density of states for a semiconducting (4, 2) chiral SWCNT, and a metallic (5, 5) armchair SWCNT. Images are from [12] with permission.

2.3 Optical Properties of SWCNTs

In general, the optical properties of carbon nanotubes refer specifically to absorption, photoluminescence, and Raman scattering. Since the electronic structure depends on the chirality of a given nanotube, experimental optical probes of the electronic structure can reveal much information about the diameter, chirality, and metallic or semiconducting nature of a SWCNT sample. In the following sections, two important optical spectroscopic techniques that are used to characterize SWCNTs are introduced.

2.3.1 Optical Absorption Spectroscopy

Optical absorption spectroscopy (OAS) measures the absorption of electromagnetic radiation. The absorption is a function of the frequency (or wavelength), due to the interaction of light with a sample. When light propagates through an absorbing medium, its intensity decreases exponentially according to the Beer-Lambert law,

$$I(L) = I_0 e^{-\alpha L c} \tag{2.8}$$

where I_0 is the intensity of the incident light, α is the absorption coefficient, L is the optical path length, and c is the concentration of an absorbing species in the material. This is illustrated in Fig. 2.5. By measuring the transmitted intensity relative to the incident intensity, the absorbance (for a given wavelength λ) is given by the following expression

$$A = -\ln\left(\frac{I}{I_0}\right) . \tag{2.9}$$

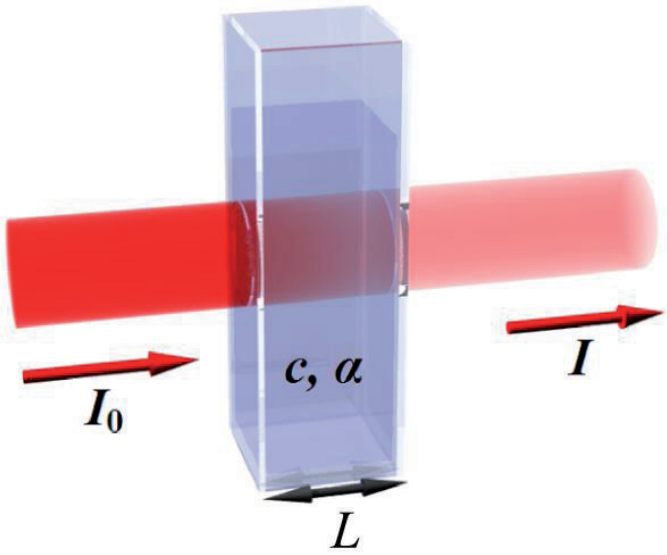

Figure 2.5 Illustration of Beer-Lambert absorption in a material with absorption coefficient α and concentration of absorbing species c. The optical path length is L, and I and I_0 are the incident and transmitted intensities, respectively. (Image used with permission from Wikipedia)

In OAS, the wavelength of the incident light is scanned and usually covers the ultraviolet, visible, and near infrared (UV-Vis-NIR) regions of the spectrum. The optical response of SWCNTs is dominated by transitions between valence and conduction bands, where momentum conservation only allows transition pairs of singularities that are symmetrically placed with respect to the Fermi level. These vertical transitions are labelled $E_{ii}\,(i = 1, 2, 3, \ldots)$. Basically, light will be absorbed when in resonance with the E_{ii} values for the (n, m) nanotubes in a sample. Despite the fact that a SWCNT has a sharply peaked density of states, the peaks that are found in OAS are broad. The dominant reason for this is due

to sample heterogeneity. An ensemble of nanotubes most often consists of many different species (n, m), each with a different set of absorption peaks, which add up to produce a broad peak that contains information about the diameter distribution in the sample. Thus OAS of SWCNTs is often used to evaluate the mean diameter (d_t) and diameter distribution of nanotubes in a sample, rather than the chiralities.

A typical absorption spectrum of bulk SWCNTs consists of three broad absorption peaks labelled E_{11}^S, E_{22}^S, E_{11}^M, which are associated with the lowest transition in S-SWCNTs, the second transition of the same S-SWCNTs, and the first peak in the joint DOS of M-SWCNTs, respectively (see Fig.2.6 (a)). The energy of optical transitions in a SWCNT is inversely proportional to the nanotube diameter. Based on the TB model, for the S-nanotubes, it follows that $E_{11}^S = 2a_0\gamma_0/d$ and $E_{22}^S = 4a_0\gamma_0/d$, where γ_0 is known as the 'tight binding nearest neighbor overlap integral'. For M-nanotubes, the energies of the optical transitions are proportional to $E_{11}^M = 6a_0\gamma_0/d$.

Although simple one-particle pictures are useful models to interpret some aspects of the experimental results[13, 14], it has become increasingly clear that Coulomb interactions also play an important role in determining the optical transition energies of SWCNTs. Both theoretical calculations and experimental measurements show that the exciton binding energies are anomalously large at about ~1 eV, in contrast to ~10 meV energies that are commonly found in 3D material, which indicates the importance of many-body (MB) effects in the quasi-1D system [15]. Essentially, the electron-electron Coulomb repulsion (electron self-energy) upshifts the one-electron energy E_{ii}^0. Simultaneously, the electron-hole Coulomb attraction (exciton binding energy) downshifts the E_{ii}^0. However, the electron self-energy (E_{SF}) exceeds the exciton binding energy (E_{EXB}), so that the net effect is that many-body E_{ii} energies are upshifted from the one-electron E_{ii}^0 energy. The effects of many-body interactions on the transition energy is illustrated in Fig. 2.6 (b).

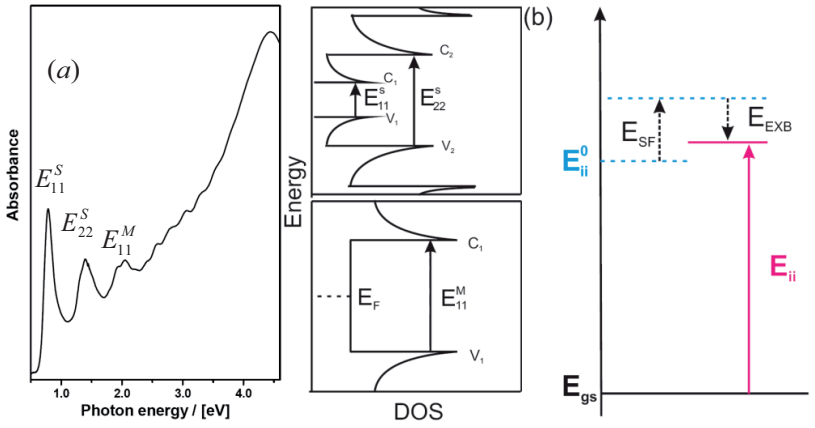

Figure 2.6 (a) A typical optical absorption spectrum of SWCNT sample showing three broad peaks that are associated with the first (E_{11}^S) and second (E_{22}^S) optical transitions for S-SWCNT and the first transition (E_{11}^M) for M-SWCNT. E_F is the Fermi level, while c and v are the conduction and valence bands, respectively. (b) Illustration of interband transitions in an exciton picture. The electron self-energy (E_{SF}) upshifts the one-electron energy (E_{ii}^0), while the exciton binding energy (E_{EXB}) downshifts the E_{ii}^0. The overall result is that the many-body transition energy E_{ii} is upshifted from E_{ii}^0.

Aside from the many-body corrections, the curvature effect and the C-C bond length optimization are also missing from the conventional TB model. It has been shown that the long-range interactions of the π orbitals are not negligible, and the curvature of SWCNT sidewalls yields a sp^2-sp^3 rehybridization in the small d_t limit[13]. The curvature effect was included in the TB model by extending the basis set to the atomic s, p_x, p_y and p_z orbitals that form the σ and π molecular orbitals, according to the Slater-Koster formalism [9]. This 'extended tight-binding' (ETB) model incorporates the TB transfer and overlap integrals as functions of the C-C interatomic distance, calculated within the frame work of a density-functional theory (DFT), and thus includes long range interactions and the effects of bond-length variations within the SWCNT sidewall [16, 17]. An ETB model which includes the many-body corrections, denoted as ETB/MB, was used in this thesis to more accurately analyze the optical properties of SWCNTs. A Kataura plot [18] was constructed based on the ETB/MB model, as shown in Fig. 2.7. Each point in this plot represents one optical transition energy E_{ii} for a specific (n, m) as a function of the diameter of the tube, d_t (top horizontal axis). The bottom horizontal axis indicates the

radial breathing mode frequency (ω_{RBM}), which will be addressed in detail in the following section.

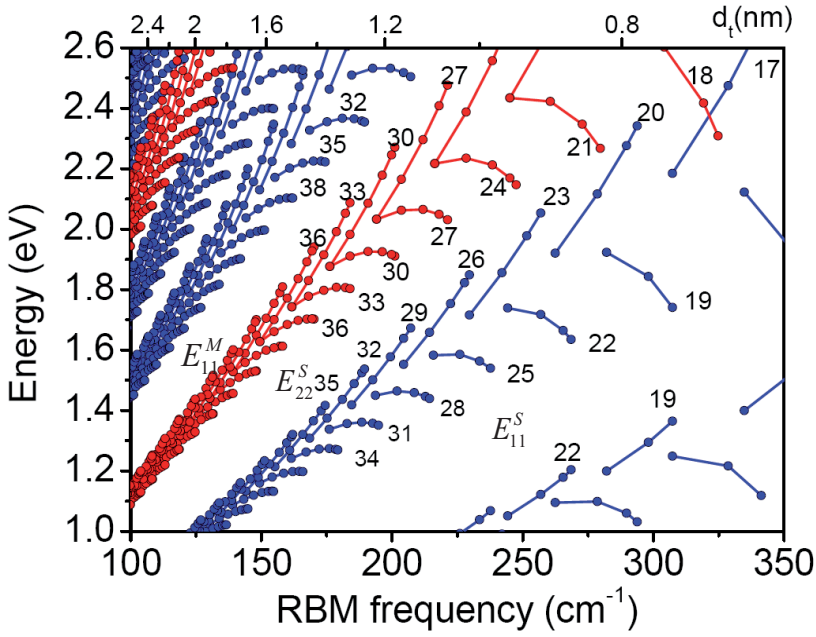

Figure 2.7 Values of optical transition energy E_{ii} as calculated with ETB/MB model for semiconducting (blue circles) and metallic (red circles) tubes vs. radial breathing mode frequency (bottom horizontal axis) and nanotube diameter (top horizontal axis). The 2n+m = constant families are joined by solid lines, and the family numbers are also indicated. The lowest two blue branches correspond to the E_{11}^S and E_{22}^S transitions of S-SWCNT, and the lowest red branch is associated with the E_{11}^M transition of M-SWCNT.

2.3.2 Resonant Raman Spectroscopy

Raman scattering refers to the inelastic scattering of a photon off of a molecule. Most scattering events are elastic (Rayleigh) processes. However, a small fraction of incident photons can be inelastically scattered, by exchanging energy with the molecule as a result of interacting with optical phonons. There are two types of Raman scattering, known as Stokes scattering and anti-Stokes scattering. In both cases, the scattering process is described by three steps consisting of (i) an absorption of the incident photon ($\hbar\nu$) into an electronic excitation of the molecule, (ii) the generation or absorption of a phonon ($\hbar\omega$), and (iii) the emission of a photon ($\hbar\nu \mp \hbar\omega$) (see Fig. 2.8).

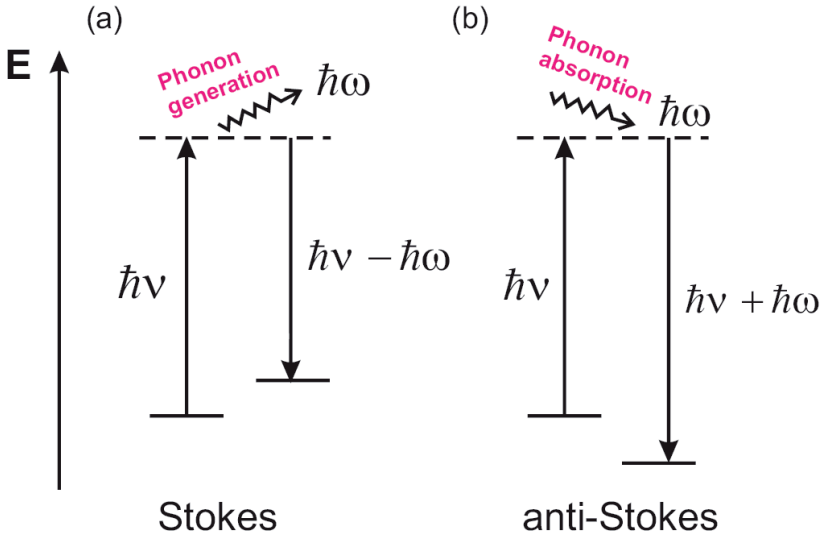

Figure 2.8 Energy level diagrams for (a) Stokes and (b) anti-Stokes Raman scattering processes. The incident photon energy is denoted by $\hbar\nu$, and by generating or absorbing a phonon with energy $\hbar\omega$, the (a) Stokes or (b) anti-Stokes scattered photon energy is $\hbar\nu \mp \hbar\omega$.

The probability for the Raman scattering process is very low (approximately 1 in 10^7 incident photons), because it involves an excitation to a virtual level that is only allowed for a very short time, in the context of the uncertainty principle. The probability is strongly increased, typically by a factor of 10^2-10^4, if the transition energy for either the absorbed or the emitted photon coincides with an electronic transition energy of the molecule. Observation of this process is called resonant Raman spectroscopy. In the case of SWCNTs, the cross section for a resonant Raman process is so large that it is even possible to analyze the vibrational modes of an individual SWCNT. Furthermore, the Raman signals detected for different excitation energies can be used to identify SWCNTs with different chiralities at resonance. This makes Raman spectroscopy one of the most important optical techniques for characterizing SWCNTs.

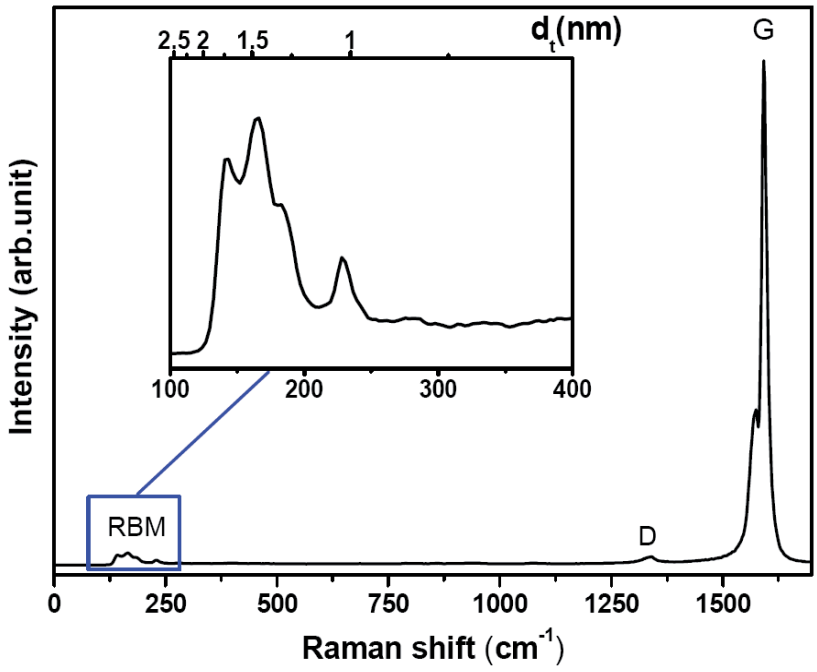

Figure 2.9 A typical Raman spectrum from a SWCNT thin film sample excited by a 533 nm laser. The inset shows the enlarged RBM peaks.

A typical Raman spectrum is shown in Fig. 2.9, where the Raman shift (i.e. the shift with respect to the excitation light wavenumber) is plotted in wavenumber units of cm^{-1}. The dominant peak located at ~1590 cm^{-1} in the figure is associated with the in-plane tangential optical phonon that involves the stretching of the bond between the two atoms in the graphene unit cell (as shown in Fig. 2.10 (a)) [10]. For this reason, this band is referred to as the graphite-like band, or simply the G band. While the G band in graphite exhibits a single Lorentzian peak at ~1582 cm^{-1}, the G band of SWCNTs splits into a lower energy G^- peak and a higher energy G^+ peak. This splitting is caused by the curvature of SWCNTs, which induces an energy difference between the axial and transverse in-plane vibrational modes. Interestingly, it has been shown that the G^- feature is strongly sensitive to whether the nanotube is metallic or semiconducting, exhibiting a Breit-Wigner-Fano (BWF) lineshape for the case of metallic nanotubes [19]. In addition, the frequency of G^+ peak is independent of both diameter and chiral angle, while the G^- feature shows a dependence on the nanotube diameter [20]. The scattering process associated with G band excitation is a first-order process, meaning that only one scattering event occurs. Second-order scattering events can occur when excited phonons are scattered by defects or inconsistencies in the crystal lattice. This shows up in the Raman spectra of SWCNTs as a small peak near 1350 cm^{-1}, which is called the

disorder band, or D-band. The ratio of the G/D modes in Raman spectra is conventionally used to quantify the structural quality of carbon nanotubes.

The last major Raman feature visible in the spectrum in Fig. 2.9 is the series of peaks below 400 cm^{-1}. These peaks are the result of a phonon excitation that is unique to SWCNTs, and they contain much information about the SWCNTs that make up the sample. The G-band mode described above is caused by a resonant in-plane vibrational mode, which is characteristic of graphite. An out-of-plane mode also exists, where the vibration is perpendicular to the lattice plane. If one imagines taking a graphene sheet supporting such an out-of-plane vibration, and rolling it into the cylindrical shape of a SWCNT, the out-of-plane vibrations become oriented radially away from the SWCNT axis, as shown in Fig. 2.10 (b). The result is a purely radial mode, where the diameter of the entire SWCNT oscillates, appearing as though it were "breathing". For this reason, this mode is known as the radial breathing mode, or RBM [12]. The Raman intensity of the RBM is strongly enhanced when the incident photon is in resonance with the energy gap E_{ii} of a SWCNT. Theoretical and experimental studies show that the RBM frequency ω_{RBM} is inversely proportional to the nanotube diameter d_t, and can be expressed by the relationship

$$\omega_{RBM} = \frac{A}{d_t} + B, \tag{2.10}$$

where A=217.8 and B=15.7 are values determined experimentally [21, 22]. Because of its dependence on the nanotube diameter, the spectrum of this mode is largely used to characterize of the diameter properties of SWCNTs.

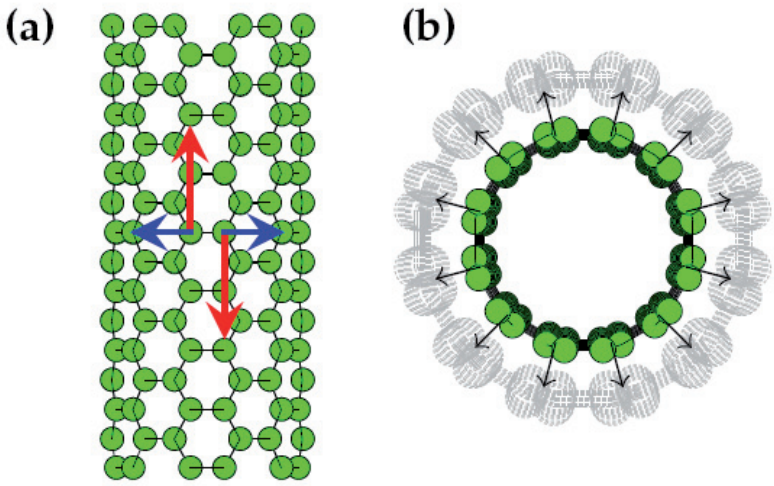

Figure 2.10 (a) the in-plane vibrational modes corresponding to the G band Raman signal, and (b) the out-of-plane vibration that gives rise to radial breathing mode excitations. Images are from [12], used with permission.

It is worth noting that, while a single Raman measurement provides information about the tubes that are in resonance with a particular laser line, it does not give a complete characterization of the distribution of diameters in the SWCNT sample. However, by collecting Raman spectra produced by many different laser lines, a good characterization of the diameter distribution can be obtained. Furthermore, when referring to the Kataura plot introduced in the previous section (Fig. 2.7), it is feasible to assign the RBMs to specific chiralities (or at least to particular 2n+m families) of SWCNTs.

3. Experimental

3.1 Synthesis Method and Techniques

In aerosol synthesis of SWCNTs, catalyst particles are suspended in the gas-phase throughout the entire SWCNT formation process. The two steps of formation of the SWCNT and the subsequent sampling are both performed directly from the gaseous phase [23]. The SWCNT samples that were studied in this thesis were synthesized in two different aerosol reactors. In both reactors, ferrocene serves as the catalyst precursor, and carbon monoxide (CO) is used as the carbon precursor. The basic chemistry and mechanisms are very similar between the two reactors, with the main difference being the dimension of each reactor. The semi-industrial scale reactor is 25 times larger than the lab-scale reactor. This enabled us to produce longer SWCNTs and at higher yield, which in turn allows for the use of the SWCNT material in additional applications.

3.1.1 Lab-scale Aerosol Reactor

In the lab-scale (LS) aerosol reactor, depicted in Fig. 3.1, CO was used as the carbon source, and ferrocene served as the catalyst precursor. The ferrocene was vaporized by passing CO gas at ambient temperature with a flow rate of 300 cm^3/min through a cartridge filled with a mixed powder of ferrocene and silicon dioxide (weight ratio $FeCp_2$:SiO_2=1:4). A stainless steel water-cooled injector probe, held at a constant 22 °C, was used to feed the precursors into the furnace (Paper III, IV). The location of the injector probe was varied (6.5-29 cm deep in the reactor) in order to control the precursor vapour heating rate as well as the residence time in the furnace. Additional CO flow of 100 cm^3/min was introduced from the outside of the water-cooled probe. The spatial temperature profiles in the reactor were measured by positioning a K-type thermocouple (SAB Bröckskes GmbH and Co., KG, Germany) at various locations in the reactor. The set temperature of the reactor furnace (T_{set}) was varied from 650 to 1000 °C. The maximum wall temperature (T) in the reactor depended on the probe position, e.g., at 6.5 cm the maximum wall temperature was 25 °C higher than the set temperature (Fig. 4.7).

At the outlet of the flow reactor, the aerosol was diluted with 12 L/min ambient temperature nitrogen (N_2), in order to reduce losses to the reactor walls from diffusion and thermophoresis. Moreover, the nitrogen can act to decrease the SWCNT agglomeration and cool the aerosol flow. Alternatively, at times the dilutor was removed and samples were collected by filtration

through nitrocellulose disk filters (Millipore Corp., USA) or through a TEM grid at the downstream of the furnace.

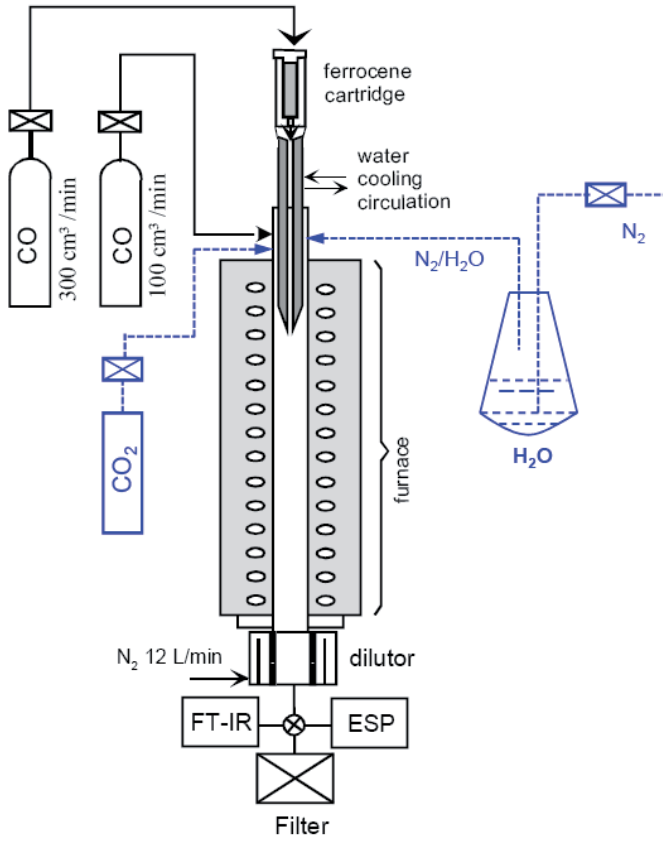

Figure 3.1. Schematic illustration of the lab-scale aerosol reactor. The inlet lines for CO_2 and H_2O vapor are marked with dotted blue lines.

The key ingredient required for the synthesis of carbon nanobuds was the presence of trace concentrations of H_2O vapour or CO_2, which acted as etching agents (Paper I). These controlled amounts of H_2O vapour and CO_2 were introduced together with CO. To obtain the H_2O vapour, a flow of a carrier gas was passed through a water saturation vessel as shown in Fig. 3.1.

3.1.2 Semi-industrial Scale Aerosol Reactor

Based on the above LS-aerosol reactor, a semi-industrial scale (IS) reactor was constructed with a 25 times scale-up in size. This allowed us to produce longer SWCNTs and with higher yield, because of the longer residence times and higher flow rates in this reactor. The temperatures were maintained at 840, 880 and 920 °C. The concentration of added CO_2 was varied from 0 to 1.2% at 920 °C (Paper II). In order to examine the effects of the residence time on the SWCNT production, the CO flow rate was varied from 2.0 to 8.0 liter per minute (lpm). It is worth noting that in order to study the effects of a particular parameter in the reactor, all other variables were kept constant while varying the given studied parameter (Paper V).

In this thesis, the maximum wall temperature will be equated with the reactor temperature, unless otherwise specified.

3.1.3 Absorber Fabrication and Laser Experimental Setup

The as-prepared SWCNT film was stamped onto highly reflecting Ag-mirrors, forming a saturable absorber mirror (SAM). Such SAMs with deposited SWCNT are ready for use without any additional processing steps. The saturable absorber mirrors of SAM1#, SAM2#, SAM3# and SAM4# refer to SWCNT films collected at CO_2 concentrations of 0.25, 0.50, 0.75 and 1%, respectively (Paper IV).

The saturable absorbers thus manufactured were then tested in Er-doped (1.56 μm) and Tm-Ho-doped (2 μm) fiber lasers having linear cavity configurations. The compact all-fiber cavities were constructed with a dichroic fiber pump coupler, a doped active fiber, and an ~80% reflecting fiber loop mirror. A polarization controller was used in the cavity for optimization of the mode-locking regime. The lasers were operated in the so-called 'net anomalous dispersion regime' that facilitates a soliton-like pulse generation.

3.2 Characterizations

3.2.1 Electron Microscopy

Transmission electron microscopy (TEM) and scanning tunneling microscopy (STM) were employed for the characterization of sample structure and morphology. A scanning electron microscope (SEM) was used to measure the bundle length of SWCNTs.

3.2.1.1 Transmission Electron Microscopy

The products collected on TEM grids by an electrostatic precipitator (ESP) were directly examined either with a field emission gun TEM (Philips CM200 FEG) (Paper I), operating with an accelerating voltage of 80 kV, or via a TEM equipped with an imaging Cs-corrector (FEI Titan 80-300), also operating with an accelerating voltage of 80 kV (Paper II-V). The electron diffraction (ED) experiment (Paper I) was carried out with the TEM (Philips CM200 FEG) operating at 80 kV together with a Gatan 794 multiscan CCD camera (1k×1k).

For the direct measurements of SWCNT diameters (Paper II, III), the microscope was carefully calibrated with a standard sample of Au particles at the magnification that was then used in the SWCNT work. In order to minimize the ambiguity of the measurement arising from the focusing deviations that might result from possible variations in the sample height, all images were focused by adjusting the heights of the specimens, while keeping the current of the objective lens constant. Under these conditions, the accuracy of the diameter measurements with high resolution TEM (HRTEM) is estimated to be about ± 0.1 nm.

3.2.1.2 Scanning Tunneling Microscope

For the STM study (Paper I), the raw soot of samples of nanobuds was sonicated briefly in dichloromethane prior to being cast onto freshly grown Au(111) substrates. High-resolution topographic STM images were subsequently obtained in ambient conditions using a Nanoscope IIIa system.

3.2.1.3 Scanning Electron Microscopy

The bundle length of the SWCNTs was measured with the SEM of a JEOL JSM-7500F microscope (Paper III).

3.2.2 Optical Spectroscopy

3.2.2.1 Optical Absorption Spectroscopy

To measure the absorption spectra of the SWCNT thin films, the sample was transferred via a dry transfer technique from filter to an optically transparent substrate, comprised of a 1 mm thickness quartz window (material: HQS300, Heraeus). The absorption spectra were recorded by a double-beam Perkin-Elmer Lambda 950 UV-Vis-NIR spectrometer. It is equipped with two excitation sources (a deuterium lamp and a halogen lamp, Papers II-V), which together cover the working wavelength range from 175 to 3300 nm. The 100% transmission baseline was calibrated without sample and reference. After the calibration, an uncoated substrate was used with a reference beam to exclude the effect of the substrate.

3.2.2.2 Photoluminescence Spectroscopy

The dispersions of SWCNTs were prepared for the photoluminescence measurement (NSI NanoSpectralyzer) (Paper III) by adding the SWCNTs to an aqueous solution of sodium dodecyl benzene sulfonate (2 wt%) surfactant, which was then sonicated with a tip sonicator (80 W output power) for 1 hour. After sonication, the suspensions were centrifuged at 10000 g for 10 minutes to precipitate the large bundles of tubes.

3.2.2.3 Raman Spectroscopy

The samples of SWCNTs which were deposited on filters or TEM grids were analyzed by Raman spectroscopy by using four different laser excitations in three Raman spectrometers equipped with cooled CCD detectors, namely a Wintech alpha300 Raman spectrometer using a Nd:YAG green laser at 532 nm (2.33 eV) (Paper I-V), an Acton SpectraPro 500I spectrometer with a He-Ne laser at 633 nm (1.96 eV) (Paper II, IV, V), and a JY-Horiba LabRAM HR 800 spectrometer using excitations at 488 nm (2.54 eV) (Paper IV, V) as well as 785 nm (1.58 eV) (Paper IV, V). Once a SWCNT was found to be in resonance with the laser energy, the full Raman spectra were recorded.

4. Results and Discussion

4.1 Local Study of a Nanobud Structure

A carbon nanobud is a hybrid material that combines fullerenes and SWCNTs into a single structure in which the fullerenes are covalently bonded to the outer surface of the SWCNTs [24]. The fullerenes on the surface of the SWCNTs are reminiscent of buds on a branch and thus called carbon nanobuds (as shown in the HRTEM image Fig. 4.1 (d)). Because of the high intensity of Raman modes arising from the SWCNTs, the Raman-active modes due to the fullerenes are very difficult to detect in the combined structure. Therefore, in this work (Paper I), we have for the first time conducted a local study of a nanobud by using a combination of Raman spectroscopy and TEM.

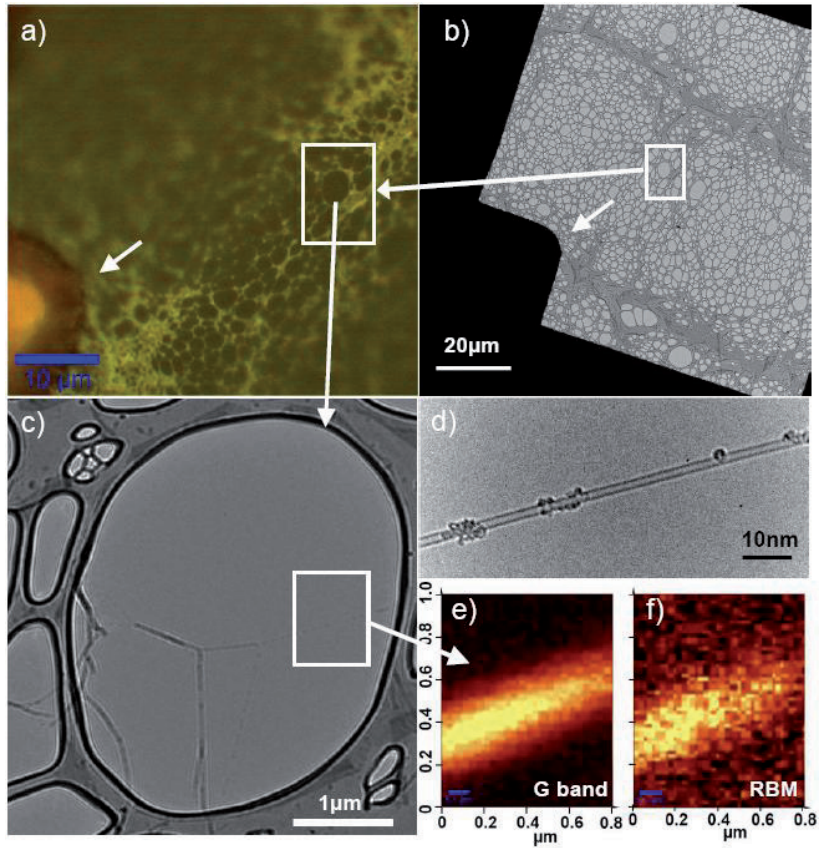

Figure 4.1. (a) Optical microscope and (b) low-magnification TEM images of the same hole in a TEM grid square. (c) An intermediate-magnification TEM image of the hole bridged by nanobuds. (d) A high-resolution TEM image of an individual SWCNT covered by fullerenes. Raman map of (e) G band (1562-1613 cm^{-1}) and (f) RBM (125-143 cm^{-1}) region on the area of 1×0.8 µm (framed in (c)).

By comparing an optical microscope image (Fig. 4.1 (a)) from the Raman spectroscopy instrument and the low-magnification TEM micrograph (Fig. 4.1 (b)), it was possible to locate the hole where the tube under study was bridging. The HRTEM image (Fig. 4.1 (d)) reveals clearly a nanobud structure, i.e. fullerenes attached to the surface of an individual SWCNT. In order to find the precise position of the nanobud, we performed Raman mapping on an area of 1×0.8 μm (framed in Fig. 4.1 (c)) on the determined hole. Raman maps were acquired by integrating the Raman signal in the 1562-1613 cm^{-1} and 125-143 cm^{-1} spectral region, which correspond to the G band (Fig. 4.1 (e)) and the radial breathing mode (RBM) (Fig. 4.1 (f)), respectively. It is easy to locate the nanobud on a submicron scale with such Raman maps. After localizing the laser spot directly on this individual nanobud structure, we recorded the Raman spectrum shown in Fig. 4.2 (a).

Regarding the freestanding individual SWCNT, the high I_G/I_D ratio (~30) implies a low defectiveness in the SWCNT. A single narrow RBM is observed at 133 cm^{-1}, and based on the equation $\omega = 223/d + 10$ [25], the calculated diameter of the SWCNT is 1.81 nm. A detected signal for 2.33 eV of incident energy means that the transition energy of the SWCNT is close to 2.33 eV. Following the references [26, 27], one can classify this SWCNT as a (16, 11) semiconducting nanotube.

On the same freestanding tube, we also conducted electron diffraction experiments. Half of the electron diffraction pattern is shown in Fig. 4.2 (b) (left). In addition to the bright spot at the center (caused by the direct electron beam irradiation), the diffraction pattern is largely composed of a set of parallel-diffracted layer-lines that are separated by certain distances from the equatorial layer-line at the center. With the use of layer-line distance analysis based on a novel concept of intrinsic layer-line spacing [28], the diffraction pattern was indexed and the chiral indices of the SWCNT were determined to be (16, 11), and the tube diameter was found to be 1.84 nm. A simulated electron diffraction pattern of a (16, 11) nanotube is produced in Fig. 4.2 (b) (right), which is in good agreement with the experimental pattern (left). The TEM and ED investigations on the same nanobud confirmed the interpretation of the Raman measurements for the SWCNT chirality assignment.

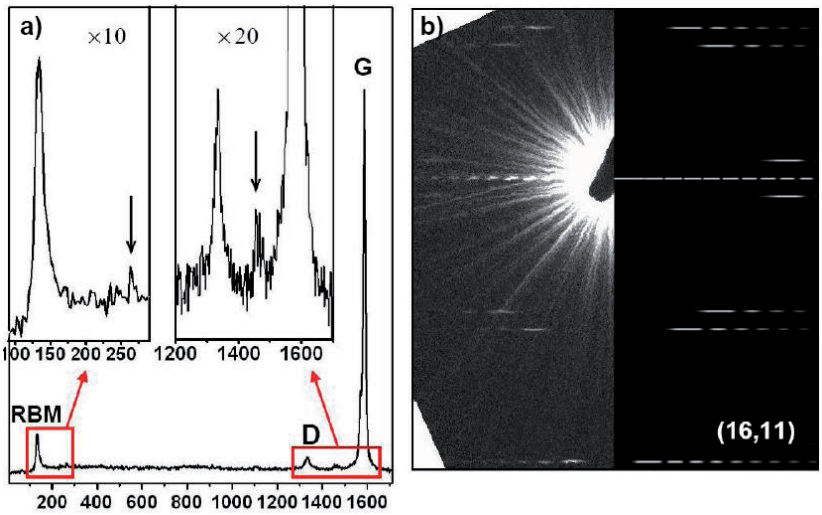

Figure 4.2. a) Raman spectrum of the nanobud structure (shown in Fig. 4.1 (d)) obtained at ambient conditions using green laser excitation (2.33 eV). The arrows indicate the fullerene features at 264 and 1465 cm^{-1}. (b) Electron diffraction pattern for the same nanotube, classified as (16,11) (left: experimental, right: simulated image).

In addition to the Raman features from the SWCNT, the Raman bands related to the vibrational modes of fullerenes are also observed at 1465 and 264 cm^{-1}. Since no Raman analysis has been done on a nanobud structure before, in order to understand the above Raman features from the nanobud, we enlighten our study with previous results involving the 'peapods structure', where fullerenes are encapsulated inside a SWCNT. For the case of C_{60} peapods, the most prominent mode is the pentagonal pinch mode $A_g(2)$, located in the Raman spectrum in a range of 1440-1480 cm^{-1} [29-31], which is often used as a probe to detect C_{60} inside of nanotubes. The excitation profiles of the $A_g(2)$ mode for a C_{60} peapod reveal one maximum at 2.5 eV [32]. When excited by the green laser at about 2.34 eV, the $A_g(2)$ mode becomes much weaker [31-33]. This case is similar to that of C_{70} peapods, where there are weak but clearly discernable peaks at 1446 and 1465 cm^{-1} when the excitation energy is about 2.38 eV [33]. In the work described in this thesis, performed at ambient conditions with an excitation energy of 2.33 eV, the Raman peaks in the range of 1440-1480 cm^{-1} are quite clear (inset of Fig. 4.2 (a)). They are associated with the typical vibrational modes of fullerenes that are located inside of a CNT, as discussed above. Additionally, a relatively weak peak at 264 cm^{-1} is observed in the spectrum (inset of Fig. 4.2 (a)). Referring to preceding studies on materials formed by nanotubes and fullerenes as parent materials (peapods) [31], the presence of this peak suggests the presence of fullerenes on the outside of the SWCNT.

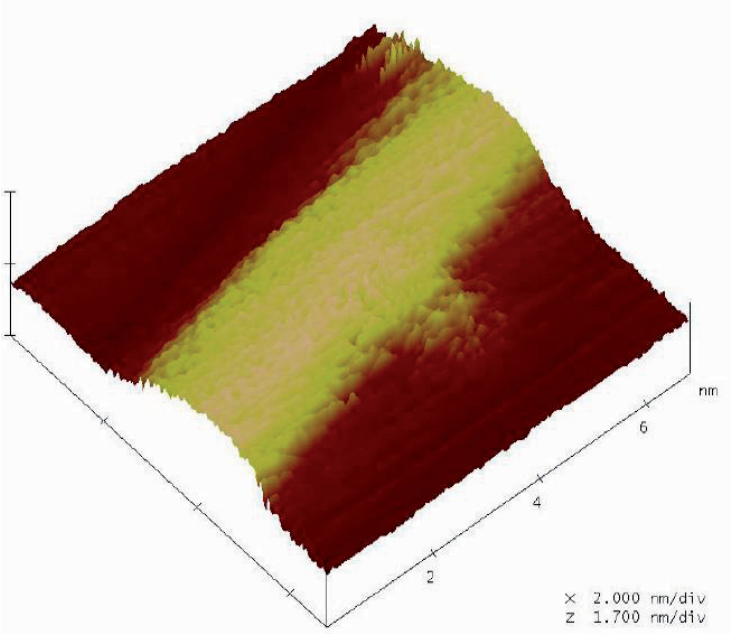

Figure 4.3. Topographic STM image of nanobud. The image size is 7×7 nm. The tunnelling current and the bias voltage are 1 nA and 1.2 V, respectively.

We also performed STM measurements on an individual nanobud structure. Fig. 4.3 shows a typical STM topographic image of the nanobud on a chiral SWCNT. The nanobud appears as a round protrusion that is attached to the nanotube wall. The nanobud attachment remained stable during high bias imaging and after continuous room temperature scans, thereby confirming the strong attachment to the nanotube wall.

4.2 Analysis Method for Size Distribution of SWCNTs based on Absorption Spectra

In Paper II, a novel method was developed to more efficiently evaluate the mean diameter and the diameter distribution in a bulk SWCNT sample using OAS. This method represents a versatile tool to analyze absorption spectra, regardless of the form or overlap of the absorption bands.

SWCNTs with different mean diameters and diameter distributions were synthesized by the IS-reactor at 920 °C, by adding different concentrations of CO_2 (denoted C1, C2, C3, C4 and C5 for CO_2 concentrations of 0, 0.4, 0.7, 1.0 and 1.2%, respectively). Fig. 4.4 shows the Raman spectra of the as-prepared samples resulting from excitation energies of 1.58, 2.33 and 2.54 eV. As expected, the Raman spectra of the samples all exhibited strong G bands (Fig. 4.4 (a)) and RBM features (Fig. 4.4 (b), (c) and (d)). The RBMs were used to probe nanotube diameters, relying on the reverse relationship of $d_t = A/\omega_{RBM} + B$ [21]. When excited with different laser energies, the relative intensity of the RBMs at the higher frequencies (indicated in the dashed frame) decreases for samples fabricated in the presence of increasing CO_2 concentration. This corresponds to a diminishing fraction of smaller diameter SWCNTs and thus implies an increase in the mean diameter.

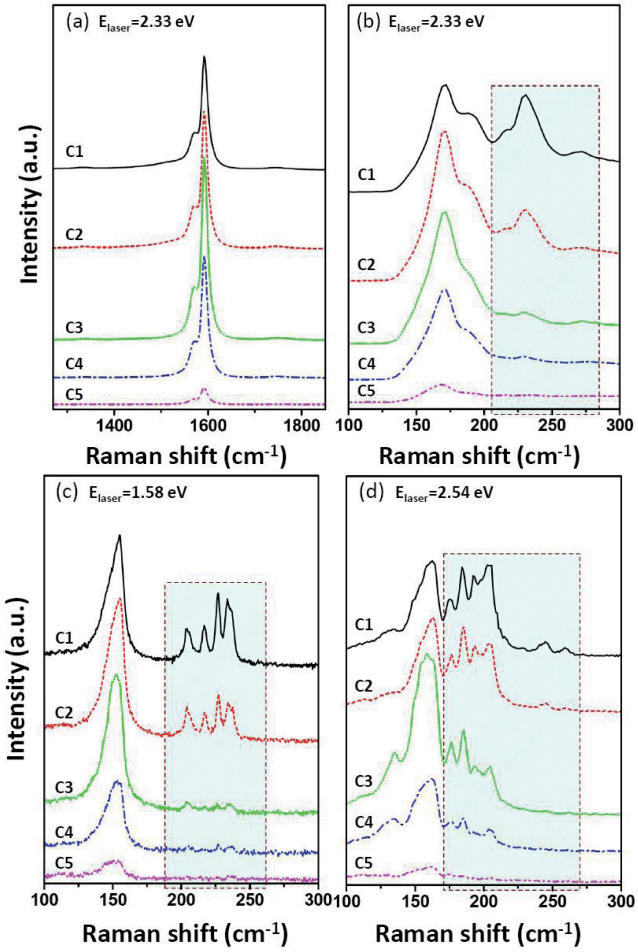

Figure 4.4 Raman spectra of SWCNT samples synthesized at 920 °C with different CO_2 concentrations under various laser energy excitations. (a) G, D bands and (b) the RBMs at 2.33 eV laser energy and the RBM spectra using lasers of (c) 1.58 eV, (d) 2.54 eV, respectively.

Raman spectroscopy only allows for the detection of SWCNTs that are in resonance with the excitation energy. Therefore, the UV-Vis-NIR absorption spectrometer is distinguished as a tool which can effectively provide the overall diameter distribution of SWCNTs. Fig. 4.5 (a) shows the as measured absorption spectra of the SWCNT thin film samples. The absorption peaks from interband electronic transitions, shown in the enlarged low energy region in the figure, strongly overlap in samples C1 and C2. Meanwhile, the absorption peaks become more resolved and narrower for the samples collected at higher CO_2 concentrations, which correspond to narrower diameter distribution in these samples. Moreover, the first absorption peak from E_{11}^{S} was observed to shift to lower energy (implying a larger mean diameter) from C2 to C4 (from top to bottom).

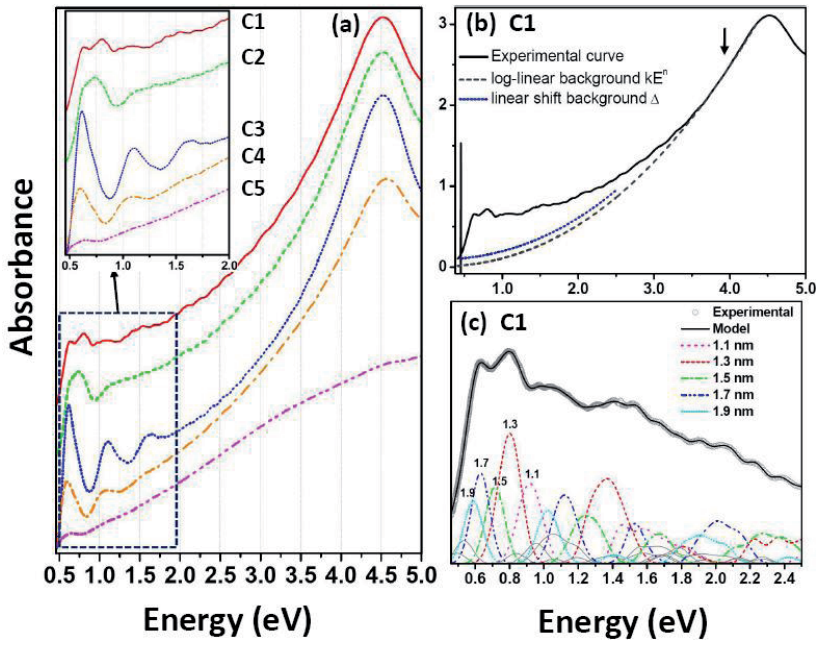

Figure 4.5 (a) Data from OAS of SWCNT samples synthesized at 920 °C with different CO_2 concentration. (b) The OAS of sample C1 along with nonlinear and linear shift of the backgrounds. The arrow depicts the data region where the background was generated. (c) The OAS of sample C1 after background subtraction (dotted grey line) and the corresponding calculated OAS (solid grey line). The contributions from the labelled diameter groups of SWCNTs are denoted by the colored dashed lines under the absorption peak areas.

Since the absorption peaks substantially overlap, it is impractical to follow the canonical approach [13, 34-40] in which one first identifies the absorption peaks and then assigns each peak to a specific transition energy. For our data, a new model was developed. The total absorption profile can be assumed to be a linear composition of background absorption and contributions from SWCNT material in the thin film sample according to

$$A\ (E) = A_{bg}(E) + A_{SWNT}(E)\,, \tag{4.1}$$

where $A_{bg}(E)$ is background absorption due to graphite, catalyst particle scattering and π-plasma absorption by carbonaceous material [21, 40, 41]. A nonlinear background model would better account for physical properties in the SWCNT absorption spectrum due to peak overlap and transition broadening [42].

The background absorption was modelled in two parts, which can be written as:

$$A_{bg}(E) = kE^n + \Delta\,, \tag{4.2}$$

where

$$\Delta = \frac{\omega_a (E_U - E\ ) + \omega_b (E_L - E\ )}{E_U - E_L}. \tag{4.3}$$

First, a log-linear model [40, 41] is applied to simulate the nonlinear part kE^n that makes up the background absorption. Then, a small positive linear shift Δ of background and the parameters in $A_{SWCNT}(E)$ are fitted. The parameters k and n are empirical, and the remaining parameters $\omega = (\omega_a, \omega_b, ..., \omega_{n,m}, ...)$ are estimated based on the absorption spectrum in the range from E_L=0.46 to E_U=2.50 eV. The result of the above process is displayed in Fig. 4.5 (b) for sample C1.

After background subtraction, the absorbance is assumed to be essentially only due to the interband electronic transitions in the SWCNT material. We then model optical absorption as a linear composition of each nanotube type:

$$A_{SWNT}(E) = \sum_{(n,m)} \omega_{(n,m)} A_{(n,m)}(E). \tag{4.4}$$

Here $\omega_{(n,m)}$ reflects the absorption probability of the (n,m)-SWCNT in the bulk (n≥m≥0). We interpret $C_{(n,m)} = \omega_{(n,m)} \Big/ \sum_{(n,m)} \omega_{(n,m)}$ as a proxy for the proportion of the amount of (n,m)-SWCNTs in the sample. $A_{(n,m)}(E)$ represents the characteristic absorption spectrum for (n,m)-tubes. This is assumed to be a sum of Gaussian line shapes that describe the broadening of each optical transition, due to the finite lifetime and finite resolution of the spectrometer:

$$A_{(n,m)}(E) = \sum_i \exp\left[-\frac{1}{2} \left(\frac{E - E^{ii}_{(n,m)}}{\Delta E} \right)^2 \right]. \tag{4.5}$$

The broadening factor (ΔE =50 meV), tested from 20 to 80 meV, was found not to be a crucial parameter for the final results. The transition energy $E^{ii}_{(n,m)}$ (i=1, 2, 3...) was taken from ETB/MB theory [17, 25, 43, 44]. All the transition energies that lie within the fitting scale (E_L- E_U) were considered in the calculation. We assume the broadening factors and absorption cross sections are both independent of the SWCNT chiralities or the different interband transitions. Those nanotubes whose diameters were in the range of 0.5-2.5 nm were considered in the fitting process.

The direct linear problem of finding the coefficients $\omega = (\omega_a, \omega_b, ..., \omega_{n,m}, ...)$ is highly ill-conditioned. A well conditioned basis

$\{A_{n,m}\}$ can contain at most on the order of forty such vectors ($E_U - E_L = 2$ eV, $\Delta E = 50$ meV). Hence, the problem is not solvable without some additional assumption. At the same time, we cannot expect to solve for any one weight accurately. Rather, we should aim for a consistent distribution under reasonable a priori assumptions that are least restrictive as possible. Consequently, we propose using a regularization scheme:

$$\min_{\omega} \left\| A(\omega) - A_{measured} \right\|_2^2 + c\Phi(\omega) . \tag{4.6}$$

Here we considered two approaches for $\Phi(\omega)$: in one, the weights of "similar" SWCNTs are correlated, as in $\Phi(\omega) = \omega^T C \omega$, where C is a positive definite correlation matrix. The other approach can be the special case of no correlation, using the 2-norm, $\Phi(\omega) = \left\| \omega \right\|_2^2$. Although both of these approaches make an assumption about the SWCNT distribution, they are much less limiting than the imposition of a Gaussian distribution on the diameters. We resort here to the second approach - we found it produces rather satisfactory results using simpler assumptions. Clearly, the regularization parameter c > 0 needs to be chosen so as to produce reasonable results. We found that c values in the range 1–3 typically achieve this.

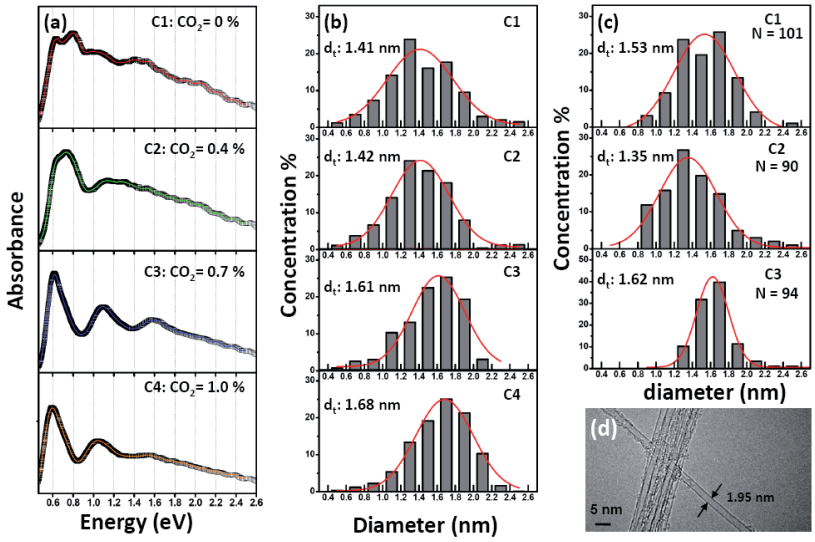

Figure 4.6 (a) OAS data after background subtraction (black dots) and fitted curves (solid lines) for the SWCNT samples. (b) The fitted diameter distribution of SWCNTs based on OAS, which give mean diameters d_t of 1.41, 1.42, 1.61, 1.68 nm for samples C1, C2, C3, and C4, respectively. (c) The diameter distributions for C1, C2 and C3 SWCNT samples as measured in HRTEM images. Red solid lines correspond to Gaussian fits, which yield a d_t of 1.53, 1.35 and 1.62 nm, respectively. (d) An example of a HRTEM image taken of sample C1.

In Fig. 4.6 (a), the dotted black lines represent the original OAS data after background subtraction, and the thin solid lines on the top denote the fitted spectra. Very small differences are observed between the fitted spectra and the experimental absorption spectra. The associated diameter distributions for the calculated spectra are drawn in Fig. 4.6 (b). The mean diameter of SWCNTs increases from 1.41 to 1.68 nm with increasing CO_2 concentration in the synthesis process. These results are in good agreement with the initial Raman studies, i.e. the relative abundance of smaller diameter SWCNTs decreases with an increase in CO_2 concentration, which suggests a narrower diameter distribution and an increase in the mean diameter.

The nanotube diameter distributions as assessed via the spectroscopy measurements described above have been validated with HRTEM, which allows direct observation and quantitative characterization of the nanotube structures. About 100 randomly isolated SWCNTs from each sample were imaged. Fig. 4.6 (d) shows an example of a diameter measurement using an HRTEM image which was taken of sample C1. The diameter histograms of the SWCNT samples as measured in HRTEM images are plotted in Fig. 4.6 (c). For sample C1, a Gaussian fit indicates a mean diameter of 1.53 nm, with 90% of the SWCNTs lying in the diameter range of 1.0-2.0 nm. The deduced diameter histogram shows the diameter distribution of the SWCNTs as being centered at 1.3 and 1.5 nm. This is in good agreement with the results obtained from OAS analysis. In the Raman results in Fig. 4.4, using different laser lines, all the RBMs spectra indeed indicate that sample C1 had the highest relative population of smaller diameter nanotubes (from 1.0 to 1.4 nm). For samples C2 and C3, the diameter diagrams derived from the HRTEM measurements yield mean diameters of 1.35 and 1.62 nm, respectively, which is also consistent with the results obtained from OAS, i.e. 1.42 and 1.61 nm, respectively. Additionally, there is a good agreement with the measured diameter distributions in samples C2 and C3. More than 77% of the SWCNTs in sample C2 have diameters in the range of 1.0-1.8 nm, and in sample C3, about 90% of the SWCNTs range from 1.2 to 2.0 nm in diameter.

4.3 Synthesis and Properties of SWCNTs

4.3.1 Lab-scale aerosol reactor

In this section, the effects of temperature, probe position and CO_2 concentration in the reactor are studied (Paper III). The experimental setup is shown in Fig. 4.7 (a). The temperature profiles were measured with a K-type thermocouple, positioned at various locations in the reactor. The set temperature T_{SET} of the reactor furnace was varied from 650 to 1000 °C. The maximum wall temperature T was a function of the probe position, e.g. at a distance of 6.5 cm the maximum temperature at the wall was 25 °C higher than T_{SET} (Fig. 4.7 (b) and (c)). As stated in the Experimental section, we use the measured maximum temperature to describe the synthesis temperature.

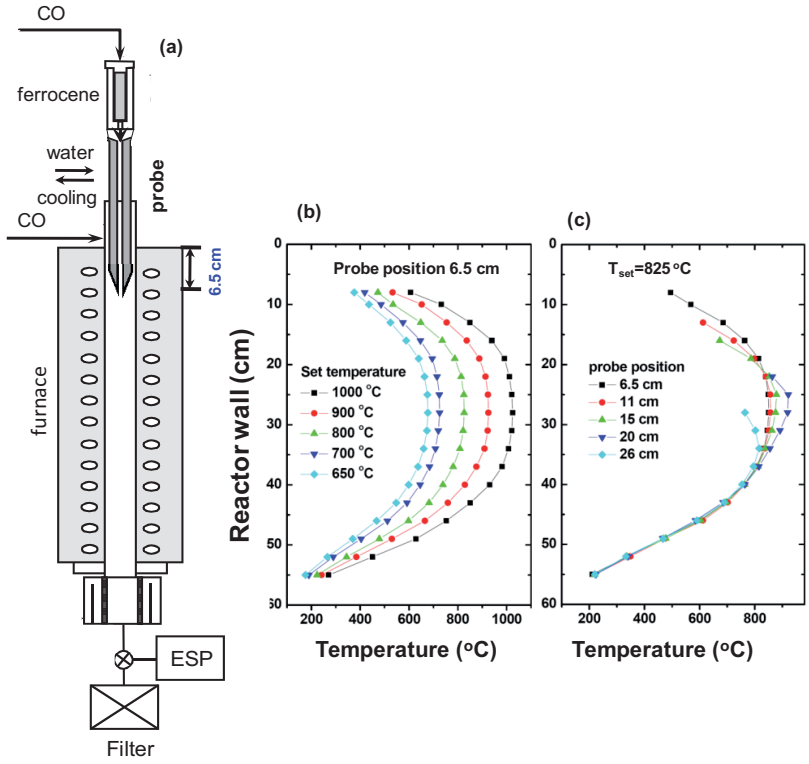

Figure 4.7 (a) Schematic of the experimental setup along with temperature profiles: (b) at water-cooled probe position of 6.5 cm as a function of T_{SET} and (c) at T_{SET} = 825 °C as a function of water-cooled probe position

Fig. 4.8 shows typical TEM images of the SWCNT samples synthesized in the LS reactor, with samples collected at temperatures of 875, 925, 975 and 1025 °C and at a probe position of 6.5 cm. The products in the samples

consist of SWCNT bundles along with some individual SWCNTs, as can be seen from the inset HRTEM image. Catalyst particles and a small amount of impurities are observed on the surface of the SWCNTs. The SWCNT bundle length depends on the temperature of the reactor. Increasing the temperature resulted in a reduction of the tube length.

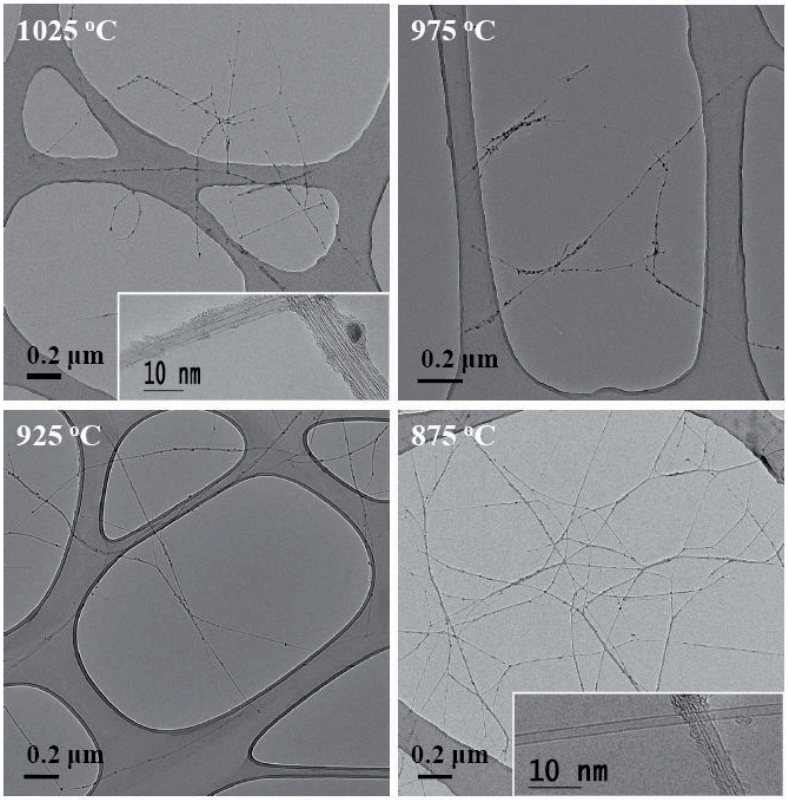

Figure 4.8 TEM images of the SWCNT samples synthesized at a probe position of 6.5 cm as a function of temperature. The inset shows a HRTEM image.

Fig. 4.9 (a) and (b) show the Raman spectra of SWCNT samples, synthesized at temperatures in the range between 875 and 1025 °C, in the RBM as well as G and D band regions, respectively. The RBM spectra excited by 2.33 eV photons in Fig. 4.9 (a) indicate similar RBM positions in the spectra in the region of 130-230 cm^{-1}. However, the central position of the most prominent RBM shifts towards the direction of higher frequency with a decrease in reactor temperature. This indicates that the relative abundance of smaller diameter SWCNTs increases with decreasing growth temperature. The Raman spectra in the region of G and D modes are normalized to the height of the G mode peaks. It is clearly evident that the intensity of D band signal decreases with increasing temperature. This is

understandable in light of the fact that defects are annealed away at higher temperatures, which results in more crystalline graphitic nanotube walls [7].

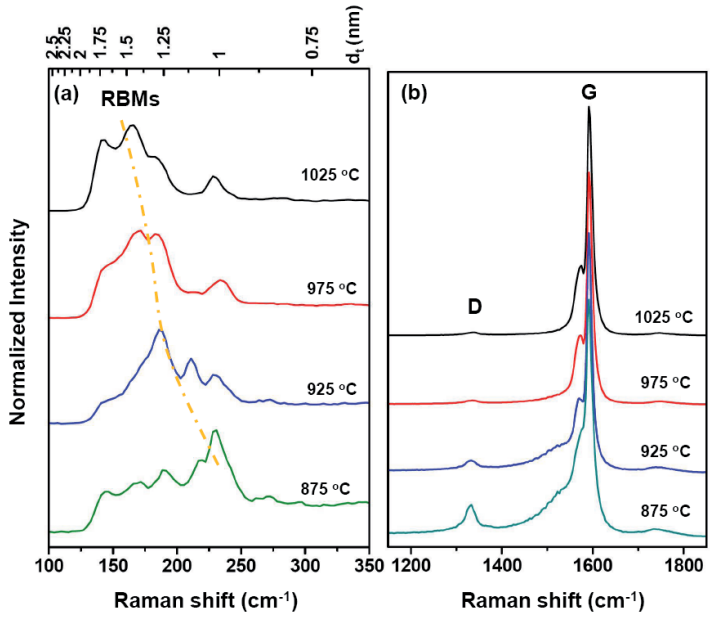

Figure 4.9 Raman spectra excited by 2.33 eV photons in the regions of (a) RBMs and (b) G and D bands for the SWCNT samples collected at a probe position of 6.5 cm as a function of temperature.

The OAS spectra for the SWCNTs that were collected at different temperatures are shown in Fig. 4.10 (a). By using the analysis method discussed in Section 4.2, the fitted diameter diagrams are shown in Fig. 4.10 (b). The mean diameter of the SWCNT samples increases from 1.2 to 1.7 nm along with the temperature. For the samples collected at 1025 and 975 °C, about 80% of the nanotubes have a diameter in the range of 1.2-2.0 nm. However, the most abundant diameter fractions are in the range of 1.6-2.0 nm and 1.2-1.6 nm for the samples collected at 1025 °C and 975 °C, respectively. For the SWCNT sample synthesized at 925 °C, the diameter diagram presents a narrower diameter distribution centered around 1.3 ± 0.2 nm. Interestingly, although the mean diameter for the sample collected at 875 °C is monotonically decreasing, and about 70% of the nanotubes lie in the diameter range of 0.8-1.4 nm, a small tail remains in the higher diameter distribution ranging from 1.6 to 2.0 nm. The photoluminescence emission/excitation (PLE) spectra (Fig. 4.11) also confirm the diameter variation as function of the growth temperature. At 925 °C, the PLE map indicates abundant semiconducting nanotubes at the emission ranges of 1300-1400 and 1500-1600 nm; while at the higher temperature of 1025 °C, the mean diameter of SWCNTs in the sample is larger and only few of SWCNTs fall within the detection range of the PL

spectroscopy, identifiable as weak bright spots in the figure. This again confirms a low yield of small diameter nanotubes in the SWCNT sample grown at high temperatures.

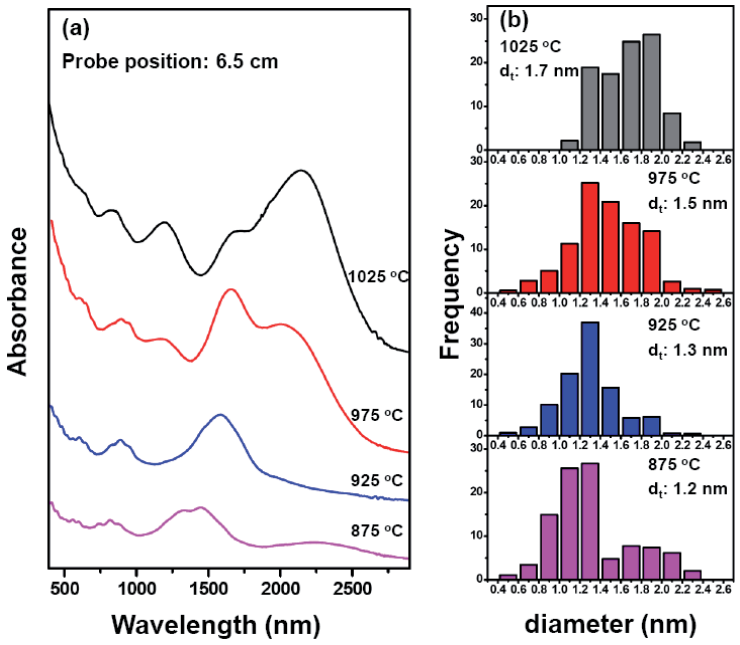

Figure 4.10 (a) UV-Vis-NIR absorption spectra and (b) the correspondence fitted diameter diagrams of the SWCNT samples collected at various temperatures. The mean diameters (d_t) increase from 1.2 to 1.7 nm along with temperature.

It has been previously observed that a reactor temperature increase results in an increase in catalyst particle size, due to a higher rate of agglomeration of primary particles, which leads to the formation of larger diameter nanotubes since the diameter of nanotubes is directly proportional to catalyst particle size [45, 46]. The results analyzed by Raman, absorption, and PL spectra in this work support this

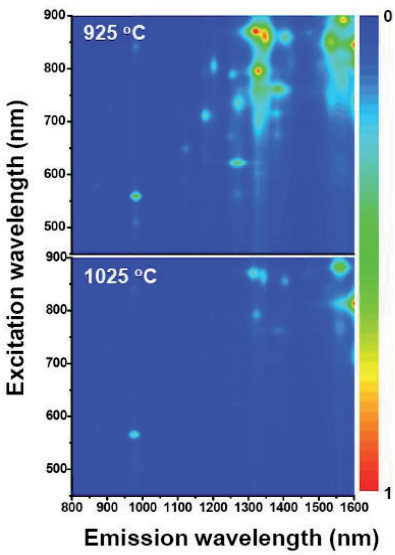

Figure 4.11 Contour plots of photoluminescence spectra of the SWCNT samples collected at T=925 and 1025 °C at probe position of 6.5 cm.

observation. Additionally, the bimodal diameter distribution of the SWCNTs shown in the absorption spectra may correlate with the bimodal size distribution in catalyst particles. Further studies on this topic are therefore warranted.

To study the effects of the water-cooled probe position on the properties of SWCNT products, the data from OAS of the SWCNT samples collected at various probe positions, at fixed set temperature of 825 °C, are shown in Fig. 4.12 (a). Interestingly, the diameter of the collected SWCNTs first increases from 1.2 nm to 1.6 nm as the probe position is continuously decreased from 6.5 cm to 23 cm (as measured from the inlet of the furnace, see experimental setup in Fig. 4.7). However, at probe positions deeper than 23 cm the mean diameter of synthesized SWCNTs starts to decrease, and is reduced to 1.2 nm when the probe position is 29 cm. We note that the position of the water-cooled probe influences both the temperature profile and the residence time in the reactor.

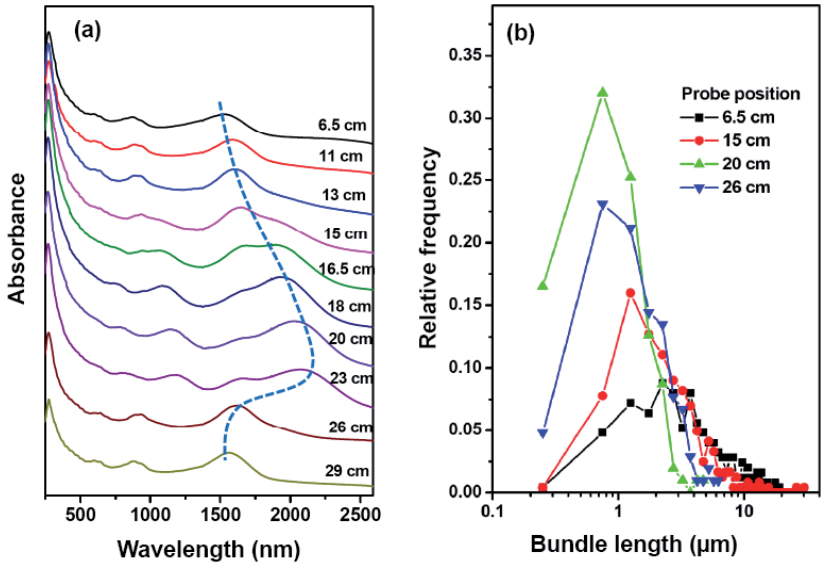

Figure 4.12 (a) UV-Vis-NIR absorption spectra and (b) bundle length distributions of the SWCNT samples synthesized at a set temperature of 825 °C as function of water-cooled probe position.

The temperature profiles shown in Fig. 4.7 (b) indicate that the maximum wall temperature of the reactor is about 25 °C higher than the set temperature when the probe position is 6.5 cm. The zone of maximum temperature is about 10 cm long around the middle of the furnace. Fig. 4.7 (c) shows that the temperature profiles vary as a function of the probe position at a fixed T_{SET} of 825 °C. The maximum wall temperature of the reactor increases from 850 to 920 °C when the position of the water-cooled

probe moves from 6.5 to 20 cm. For probe positions deeper than 26 cm, the maximum temperature of the reactor begins to decrease. The reason can be found in the fact that the reactor is a two-heating zone reactor, which is controlled by two thermocouples located at 21 and 36 cm, respectively. The deeper the probe position, the higher the cooling rate. and as a result the heating elements of the furnace work at higher power levels to keep the set temperature fixed at 825 °C at 21 cm. This results in a higher maximum wall temperature in the middle of the furnace, and therefore the maximum wall temperature increases with the probe position. However, when the probe position extends beyond the middle of the furnace (probe is deeper than 26 cm), the whole upper part of the heating zone is cooled by the probe, which produces a lower maximum wall temperature in the reactor. As shown in Fig. 4.7 (c), the maximum wall temperature of the reactor is 815 °C for a probe position of 26 cm (T_{SET} = 825 °C). These temperature profiles explain the results of the absorption measurements in Fig. 4.12 (a), i.e. the mean diameter of SWCNTs first increases with the probe position and then decreases after the probe position exceeds 23 cm.

The bundle length of synthesized SWCNTs was also found to be dependent on the probe position, as shown in Fig. 4.12 (b). The length of SWCNTs first decreases with the probe position, but then increases after a probe position of 26 cm is reached. It is believed that the length of SWCNT can be controlled by both the residence time and the temperature in the reactor. On the basis of in-situ sampling experiments, it was found that the growth of SWCNT stops when the temperature is higher than 928 °C, due to the thermodynamic restriction of the CO-disproportionation reaction at high temperatures [6]. A similar experimental phenomenon was observed in another aerosol system (a 'hot wire generator' reactor), where the growth of SWCNTs stops at a temperature of 908 °C [47]. When the temperature is below 900 °C, the SWCNTs continuously grow throughout the reactor, and remain in the high temperature zone for a longer time. This also explains the observation made in TEM images (Fig. 4.8) that the bundle length increases with decreasing reactor temperature. When the maximum wall temperature is 900 °C, the residence time in the reactor plays an important role in determining the length of the resultant SWCNTs. As shown in Fig. 4.12 (b), the average bundle lengths of SWCNTs collected at probe positions of 6.5, 15, and 26 cm are 5.4±4.1, 3.6±3.5, and 1.8±1.2 μm, respectively. However, for the SWCNT sample synthesized at a probe position of 20 cm, the bundle length is the shortest, with about 1.2±0.8 μm, due to the high maximum wall temperature of about 920 °C in the reactor. Therefore, by simply moving the probe position, the residence time and temperature profile of the reactor can be changed. This provides an efficient means for

altering the mean diameter, diameter distribution, and the length of SWCNT products.

CO_2 also plays an essential role in the growth of SWCNT structures (Paper IV). Raman spectroscopy performed at excitation energies of 1.96 and 2.33 eV was used to characterize SWCNTs that were grown with different CO_2 concentrations (Fig. 4.13). The intensity ratio between G and D bands (I_G/I_D) is used as an indicator of the quality of the SWCNT samples [48], and are plotted in the insets of Fig. 4.13 (b) and (d), respectively. They show that the quality of SWCNTs is improved by increasing the CO_2 concentration. However, the growth of SWCNTs was significantly suppressed at a CO_2 concentration of 1.20% in the process, and growth completely vanished at even higher concentrations.

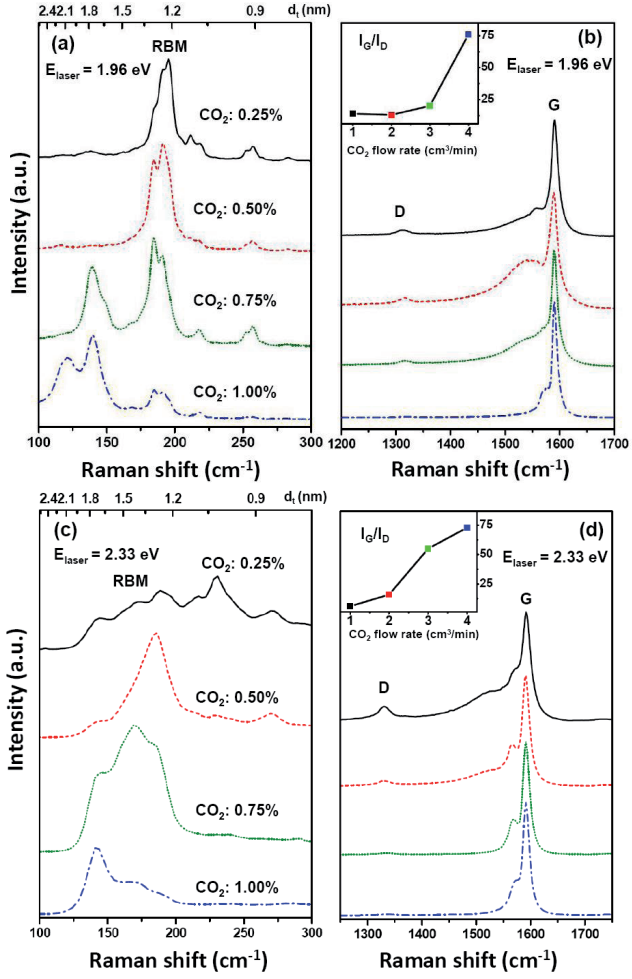

Figure 4.13 Raman spectra produced by different excitation laser energies for SWCNT samples synthesized at 880 °C with different CO_2 concentrations. (a) and (b) show RBMs and G, D bands excited by 1.96 eV, (c) and (d) show RBMs and G, D bands excited by 2.33 eV. The insets depict the I_G/I_D ratio as a function of CO_2 flow rate.

When excited by the laser energy of 1.96 eV (Fig. 4.13 (a)), the RBM peaks are mainly located in the region of 180-220 cm^{-1} for the samples produced at CO_2 concentrations of 0.25 and 0.50%. It is worth noting that the peak at the lower frequency of 185 cm^{-1} is more pronounced in the sample collected at a CO_2 concentration of 0.75%. For the samples collected at CO_2 concentrations of at 0.75 and 1.00%, new RBM peaks in the range of 100-150 cm^{-1} appear, indicating enrichment with larger diameter tubes in these samples. Moreover, the peaks in the higher frequency region of 180-220 cm^{-1} are significantly suppressed for the SWCNTs grown at 1.00% of CO_2. This indicates that the abundance of larger diameter nanotubes increases with CO_2 concentration. Additional RBM analysis at 2.33 eV excitation (Fig. 4.13 (c)) suggests similar results, derived from the downshift of the RBM peaks with an increase in CO_2 concentration.

The absorption spectra of the SWCNT samples collected at 880 ^oC under different CO_2 concentrations are shown in Fig. 4.14 (a). It can be seen that the absorption peaks significantly shift to longer wavelengths with an increase in CO_2 concentration. This indicates that the diameter of SWCNTs increases with CO_2 concentration in the reactor. Using the same fitting program as before, the derived mean diameters of the SWCNTs are 1.2, 1.3, 1.5 and 1.9 nm for CO_2 reactor concentration of 0.25, 0.50, 0.75, and 1.00%, respectively (Fig. 4.14 (b)).

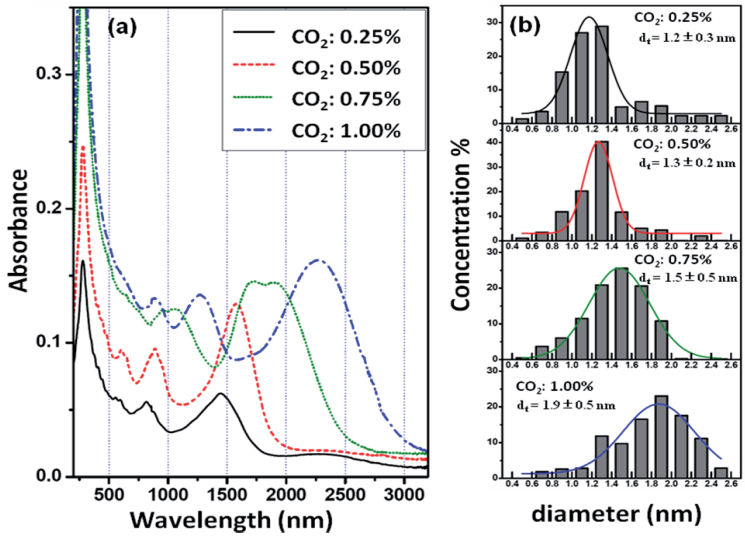

Figure 4.14 (a) The absorption spectra for SWCNT samples synthesized at 880 °C with different CO_2 concentrations. (b) The evaluated diameter distributions of SWCNT samples produced with different CO_2 concentrations based on OAS, which give mean diameters d_t of 1.2, 1.3, 1.5, 1.9 nm, respectively.

Analysis of both Raman and absorption spectra shows that increasing the concentration of CO2 in the reactor results in the growth of SWCNTs with larger diameters. The nucleation of CNTs is believed to occur on solid iron supersaturated by carbon. Carbon released on the surface forms a graphitic cap (Fig. 4.15) - a CNT nucleation site (a CNT embryo). If an etching agent such as CO_2 is present in the system, CNT embryos with low curvature have a higher survival probability. Conversely, embryos with high curvature are easily etched due to the inverse Bouduard reaction (Eq. 4.7). Furthermore, the CNT embryos which survive begin to grow by feeding carbon into the concave regions, where carbon atoms are consumed due to their incorporation into the hexagonal CNT network. This leads to the creation of a carbon concentration gradient in the particle, which provides a continuous flux of carbon atoms through the catalyst particles from the surface to the region of growth in the CNT. The concave region is preserved during the growth of the CNT, since the CNT walls are much stiffer than the iron particle. The part of the particle that is embedded inside the growing CNT during the initial stage is pulled outwards from inside of the CNT, due to the surface tension of the catalyst particles. The last frame in Fig. 4.15 (a) corresponds to the conditions of steady-state growth of CNTs. It is worth mentioning that this proposed picture of CNT growth mechanism is valid not only for SWCNTs, but also for the growth of multi-walled CNTs synthesized by the substrate CVD method [49, 50].

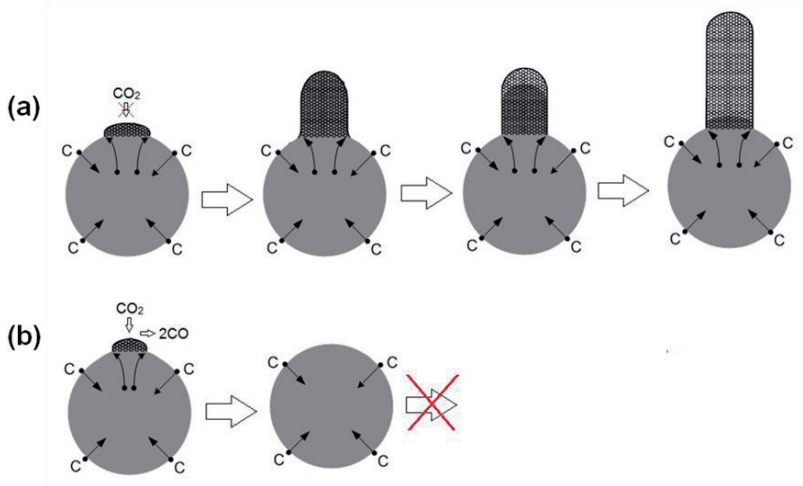

Figure 4.15 Schematic presentation of CNT growth mechanism: (a) "surviving" of an embryo of large diameter CNT and its subsequent growth and (b) destruction of smaller diameter tubes due to inverse Bouduard reaction at highly curved carbon surfaces.

Additionally, considering the I_G/I_D ratio from Raman analysis, one can conclude that a small amount of CO_2 can assist in the synthesis of high

quality SWCNTs. From these results, we believe that a well-defined amount of CO_2 also plays an etching role against the amorphous carbon coated on the surface of catalyst particles and SWCNTs, thereby enhancing the activity and lifetime of the catalysts in nanotube growth, resulting in an improved quality of carbon nanotubes [51]. However, the growth of SWCNTs was found to be significantly suppressed at CO_2 concentrations higher than 1.20%. This might be explained by an excessive etching of the carbon nanotube caps that prevents the CO disproportionation by shifting the equilibrium reaction to the left:

$$CO_{(g)} + CO_{(g)} \Leftrightarrow C_{(s)} + CO_{2(g)}, \quad \Delta H = -169kJ/mol. \tag{4.7}$$

4.3.2 Semi-industrial Scale Aerosol Reactor

In Paper V, the influence of various reactor parameters (temperature, CO_2 concentration and flow rate) on the properties of synthesized SWCNTs was investigated in detail for the semi-industrial scale (IS) aerosol reactor. Compared to the previous LS-reactor, in the IS-reactor the SWCNTs were formed at higher yield and with longer bundle length, because of longer residence time and higher gas flow rates in the IS-reactor. Fig. 4.16 shows typical TEM images of SWCNTs formed in this IS-reactor. The overview TEM images show that the nanotube bundles produced in this reactor are quite long, and only a small amount of inactive catalyst particles are present in the product. The higher magnification TEM images reveal that the samples consist of individual or bundle SWCNTs, and the sample synthesized at 920 °C presents cleaner SWCNT surfaces than do the other two samples.

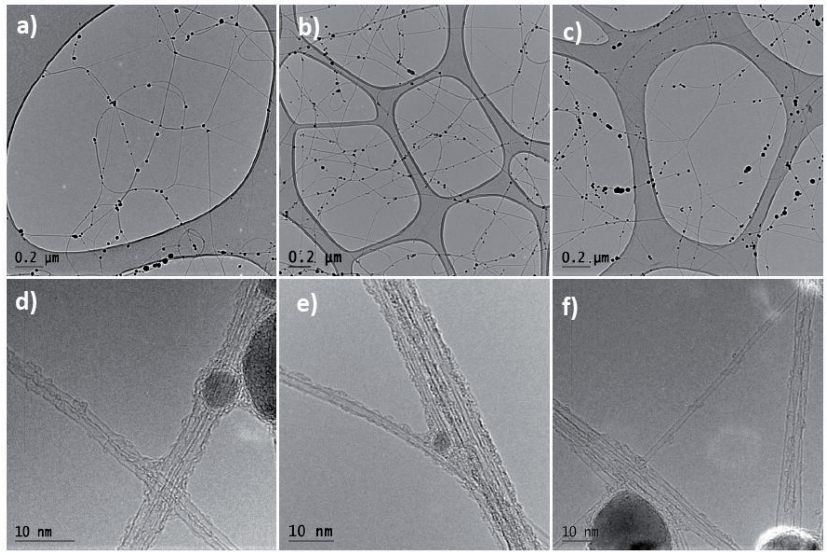

Figure 4.16. Low and high magnification TEM images of SWCNTs synthesized in the IS-reactor without adding CO_2 at (a) and (d) 840 °C, (b) and (e) 880 °C, (c) and (f) 920 °C.

When compared with the findings for the LS-reactor, the reactor parameters of CO_2 concentration and temperature seem to produce similar effects on the properties of SWCNT samples in the IS-reactor. The addition of small amount of CO_2 plays an essential role in the selective etching of small-diameter nanotubes and in the purity of SWCNTs that are produced. Increasing the synthesis temperature results in the formation of larger catalyst particles due to a higher agglomeration rate, thereby forming larger diameter nanotubes. Additionally, the flow rate of CO is also a parameter that has an influence on the nature of SWCNT products.

Fig. 4.17 shows the Raman spectra of SWCNTs collected at CO flow rates of 2.0, 4.0 and 8.0 lpm at a temperature of 880 °C. The inset to Fig. 4.17 (a) shows the intensity ratio of I_G/I_D as a function of CO flow rate, produced with an incident laser energy of 2.33 eV. The intensity ratios of G and D bands are all greater than 50, which indicates a high quality for these SWCNT samples. The highest ratio is obtained for the sample synthesized at a CO flow rate of 2.0 lpm. Similar RBM spectra are observed in Fig. 4.17 (b) when the tubes were excited by 2.33 eV. While using a excitation energy of 1.58 eV, the intensity of RBMs increases in the range of 200-250 cm^{-1} as a function of the CO flow rate. Similarly, the data resulting from excitation energies of 1.96 and 2.54 eV show the relative intensity of RBMs located at higher frequencies is increased when the CO flow rate is 8 lpm. This implies an increase in the relative concentration of smaller diameter nanotubes with higher CO flow rates.

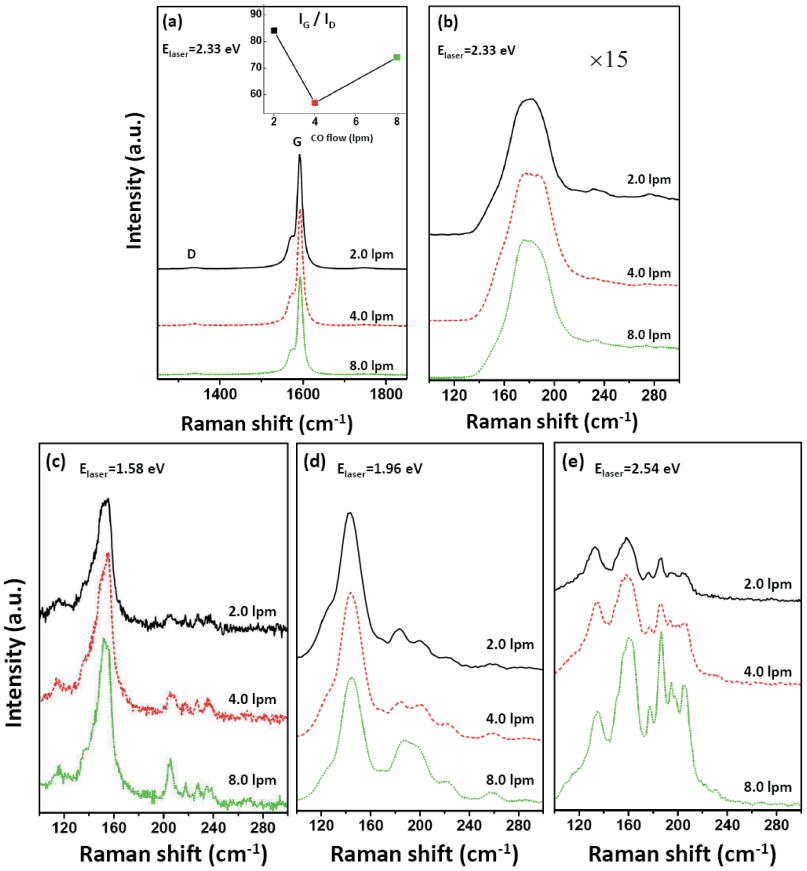

Figure 4.17 Raman spectra of SWCNT samples showing (a) G, D bands excited by 2.33 eV and RBM bands excited by (b) 2.33 eV, (c) 1.58 eV, (d) 1.96 eV and (e) 2.54 eV energies as a function of CO flow rate, with a constant CO_2 concentration of 1.2%. The inset in Fig. 4.17 (a) shows the calculated I_G/I_D ratio as a function of CO flow rate.

The absorption spectroscopy measurements were performed to complete the picture of the diameter distribution for this set of SWCNT samples. As shown in Fig. 4.18 (a), the lowest energy absorption peaks of the three samples exhibit a bimodal structure, and the relative intensity of the peak at about 0.7 eV increases with the CO flow rate. Fig. 4.18 (b) and (c) display the fitted absorption spectra (solid lines) along with the spectra after background subtraction (black dotted lines) and the calculated diameter distributions, respectively. For the SWCNT samples collected at a CO flow rate of 2.0 and 4.0 lpm, the two bimodal distributions both consist of diameter fractions that are most abundant in the range of 1.2-1.6 nm and 1.6-2.2 nm; however, the relative concentration of the two fractions changes with the flow rate. The percentage of nanotubes with a diameter in the range of 1.2-1.6 nm increases from 21% to 32% when the CO flow rate increases from 2.0 to 4.0 lpm. For the SWCNT sample synthesized at a CO

flow rate of 8.0 lpm, the concentration of nanotubes with smaller diameters (1.0-1.6 nm) increases dramatically up to 50%. Furthermore, the mean diameters are 1.8, 1.7 and 1.6 nm for the SWCNT samples synthesized at CO flow rates of 2.0, 4.0 and 8.0 lpm, respectively. Therefore, it is clear that the fraction of smaller diameter nanotubes increases with an increasing CO flow rate. These results obtained from absorption spectra are in good agreement with the analysis of Raman spectra. Namely, with an increase in CO flow rate, the relative fraction of smaller diameter nanotubes increases, which results in a decrease of the mean diameter.

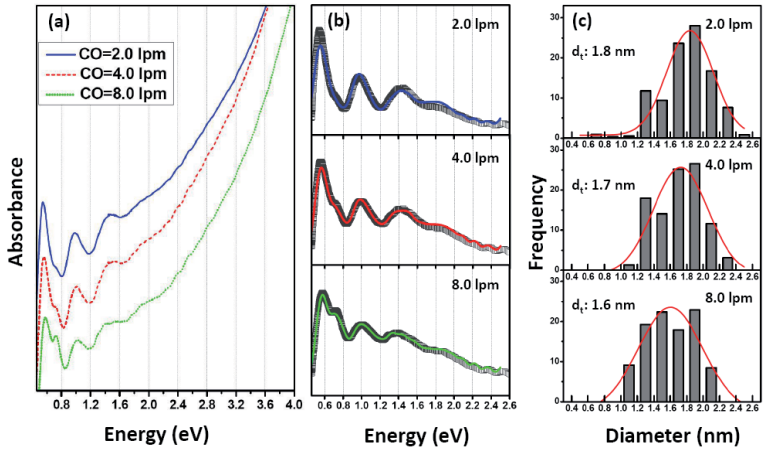

Figure 4.18 OAS data for SWCNT samples (a) before and (b) after background subtraction (in black dots), along with the fitted curves (in colored solid lines), and (c) the corresponding fitted diameter distributions of SWCNT samples as a function of CO flow rate with a constant CO_2 concentration of 1.2%. The mean diameters d_t of the samples are 1.8, 1.7 and 1.6 nm at CO flow rates of 2.0, 4.0 and 8.0 lpm, respectively.

The CO flow rate influences both the ferrocene heating rate and the residence time in the reactor. Lower flow rates lead to lower heating rates and a longer residence time, which provides a greater opportunity for Fe catalyst particles to collide and to aggregate and form larger particles. As discussed in the previous section, larger catalyst particles result in the formation of SWCNTs with larger diameters. Therefore, lower flow rates result in a larger mean diameter of SWCNTs, as observed in the Raman and absorption spectra. Additionally, the highest purity of a SWCNT sample is obtained at a CO flow rate of 2.0 lpm. This may also be due to the resultant longer residence time in the high temperature zone of the furnace. The impurities and amorphous carbon can be annealed and etched away during a longer exposure time to the high temperature, since the CO disproportonation reaction is significantly shifted in the direction of initial components.

4.4 Optical Application of SWCNTs as Saturation Absorber

SWCNTs with a specific desirable diameter are required for various applications, particularly in the area of electronics and photonics, since the diameter is an essential characteristic that determines the electronic and optical properties of SWCNTs. Successful implementation of CNTs in ultrafast lasers requires an adequate control of their absorption properties to ensure self-starting, short-pulse generation, low-threshold power operation at particular wavelengths. The fabricated SWCNT films with the desirable nanotube diameters used as SAMs were tested in Er-doped (1.56 μm) and Tm-Ho-doped (2 μm) fiber lasers having linear cavity configurations, as shown in Fig. 4.19.

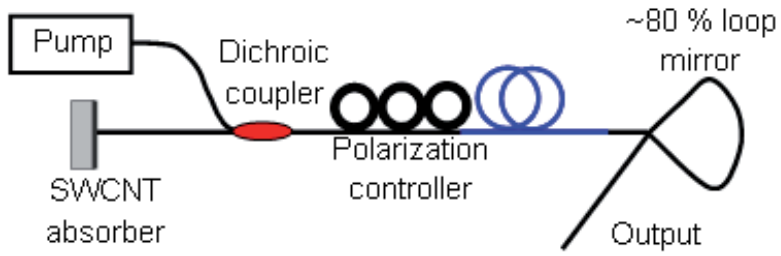

Figure 4.19 Principle schematic of mode-locked fiber laser.

Table 4.1 Measured nonlinear parameters for SWCNT films at 1560 nm.

Thin films	Nonsaturable loss (%)	Modulation depth (%)	Saturation fluence ($\mu J/cm^2$)
SAM#1	2.0	0.5	300
SAM#2	6.5	2.6	200
SAM#3	7.0	1.5	200
SAM#4	4.0	1.0	150

Table 4.1 summarizes the results of the nonlinear reflectivity measurements for the four SAMs, i.e. SAM#1, SAM#2, SAM#3 and SAM#4 corresponding to SWCNT films prepared by the LS-reactor operating with CO_2 concentration of 0.25, 0.50, 0.75, 1.00% at 880 °C, respectively (see Fig. 4.14). The variation of the nonlinear absorption among the different films is obviously due to different SWCNT diameter distributions in the films. The SAM#2, with an average nanotube diameter of 1.3 nm (the red

curve in Fig. 4.14), exhibited a strong absorption at ~1.56 μm and was chosen for the experiment with the erbium fiber laser. The nonlinear reflectivity response of this SAM reveals a modulation depth, nonsaturable loss, and saturation fluence of ΔR=2.6%, α_0=6.5% and F_{sat} ~200 μJ/cm², respectively, as determined by the measurement results shown in Fig. 4.20. The modulation depth, beneficial for self-starting pulse operation in the laser, is increased by accurate SWCNT parameter optimization, as compared with our earlier results that involved a broadband SWCNT-based saturable absorber and which was based on non-optimized SWCNTs [52]. The Er-doped fiber. having a length of ~2 m, is pumped with a 980 nm single mode pump diode. The SWCNT enables a self-starting mode-locked operation with the low threshold in pump power of ~25 mW. The optical pulse spectrum contains no sign of continuous wave components and is shown in Fig. 4.21 (a). The measured spectral width is 6.8 nm. The inset to Fig. 4.21 (a) depicts the corresponding autocorrelation trace, together with a sechant²-fitting (red line). In this measurement, the pulse width is found to be 0.43 ps, determined by an average cavity dispersion of ~-0.18 ps². The pulse repetition rate is 15.0 MHz, and the time-bandwidth product is 0.36. The maximum average output power of the laser in the single pulse regime is ~3 mW, corresponding to pulse energies of 0.2 nJ.

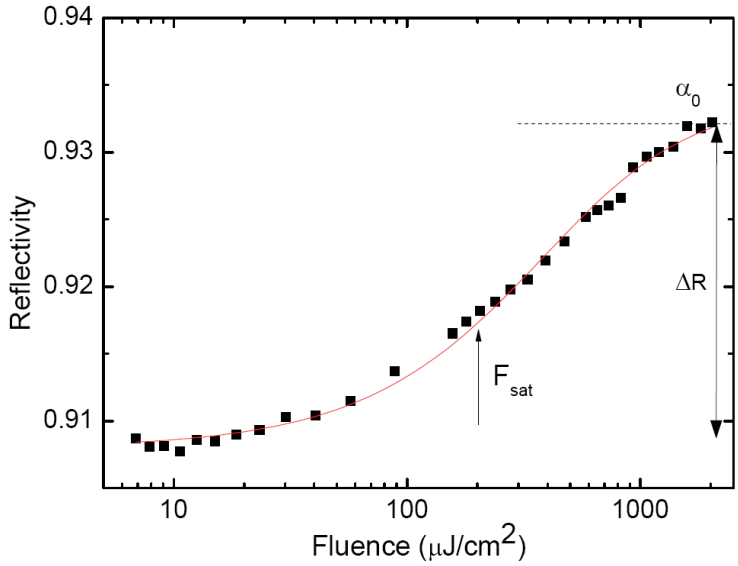

Figure 4.20 Measured nonlinear reflectivity at 1560 nm of the SWCNT film collected with a 0.5% CO_2 concentration in the reactor.

Although the three other SAMs presented in Table 4.1 were also found to be capable of starting mode-locked operation, they offered a higher lasing threshold of ~45 mW when compared with SAM#2. It is observed that the

0.25, 0.75, and 1.00% CO_2 samples also provoke a tendency to Q-switched mode-locking operation, and cause a pulse broadening to 0.55-0.6 ps. This is due to their smaller modulation depths and smaller ratios between modulation depth and nonsaturable loss in the SAMs #1, #3 and #4. The modulation depth of the SWCNT film increases in the close vicinity to the linear absorption peak maximum, while the nonsaturable losses remain at relatively low levels, which is beneficial for short pulse self-starting mode-locking operation.

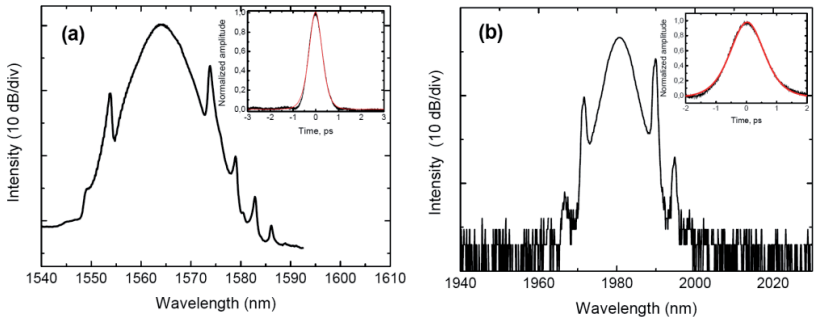

Figure 4.21 Optical spectra of the (a) erbium-doped and (b) Tm-Ho-doped fiber laser, mode-locked using SWCNTs. The insets show the autocorrelation trace with sech²-fitting (red line).

The Tm-Ho-doped fiber, having a length of ~1.7 m, is pumped using a 1.56 μm single mode Er-doped fiber laser. The SAM#3 with an absorption peak at 2 μm (see Fig. 4.14, green line) enables self-starting mode-locking operation with a power threshold of ~150 mW. The laser produces 0.84 ps nearly transform-limited pulses, with a time-bandwidth product of 0.38. The spectrum of the laser and the corresponding autocorrelation trace with sech²-fitting are shown in Fig. 4.21 (b). The laser cavity repetition rate and average cavity dispersion were found to be 32.2 MHz and ~-0.53 ps², respectively. The use of SAM#3 and SAM#4 demonstrated self-starting pulse regimes with similar pulse widths. The other films, with lower absorption at 2 μm, were unable to start passive mode-locking at all. The nonlinear reflectivity and mode-locking experiments thus performed indicate clearly the effect and the importance of precise diameter-controlled synthesis of SWCNTs.

5. Conclusions

The local study of an individual freestanding nanobud was conducted by means of Raman spectroscopy, in combination with TEM. The Raman studies of this single nanobud structure provided, for the first time, evidence of the simultaneous presence of SWCNT and fullerenes. The TEM and ED investigations on the same nanobuds are in good agreement with the Raman results, which confirms the Raman measurement interpretation for the chirality assignment of the SWCNT and the presence of fullerenes on the surface of the SWCNT.

A new optical analysis method was developed to efficiently evaluate the mean diameter and diameter distribution in any bulk SWCNT sample, using data from optical absorption spectroscopy. Raman spectroscopy and HRTEM techniques were employed to validate these results. Comparisons between the different techniques suggest that absorption spectroscopy of bulk SWCNTs is very efficient in assessing nanotube diameter distributions, regardless of the appearance of absorption bands and the form of diameter distributions. This method is expected to be extended to assign the chirality distribution of SWCNTs in case of appearance of more featured absorption peaks.

The detailed parametric analysis of SWCNTs synthesized in both lab-scale and semi-industrial scale aerosol reactors was performed by utilizing a combined study of Raman, photoluminescence, optical absorption spectroscopies and electron microscopy. The scaled-up (semi-industrial scale) reactor allowed us to produce long SWCNTs with high yield, because of the longer residence times and higher flow rates in that reactor. Depending on different growth conditions, involving parameters such as CO_2 concentration, temperature, CO flow rate, and water-cooled probe position, the mean diameter of tubes in a SWCNT sample can be adjusted from 1.1 to 1.9 nm and from 1.2 to 1.8 nm in the lab-scale and semi-industrial scale aerosol reactor, respectively. The purity and bundle length of SWCNTs can also be tuned by variation of these growth parameters. The related growth mechanisms that explain these results were discussed in detail.

The growth of SWCNTs with well controlled diameters creates the possibility for adjusting the properties of SWCNTs to meet specific needs in specific applications. We demonstrated the application of SWCNT thin

films with optimized tube diameters to serve as saturable absorbers, after being stamped onto a highly reflecting Ag-mirror. Sub-picosecond mode-locked fiber laser operation at ~1.56 μm and ~2 μm with these absorbers demonstrated improvements in the laser performance after the SWCNT properties were optimized.

On the base of the achievements that we made in this thesis, i.e., diameter and length controlled growth of SWCNTs, the direct selective growth of SWCNTs with variable metallicity can be expected as a next goal by the advanced aerosol reactor. The selective growth of semiconducting or metallic SWCNTs is very crucial for the wide various applications of which some require the properties of semiconducting nanotubes, whereas others exploit the properties of metallic nanotubes.

6. References

[1] M. S. Dresselhaus, G. Dresselhaus, P. Avouris, *Carbon Nanotubes Synthesis, Structures, and Applications*, Springer, Heidelberg 2001.

[2] A. Moisala, in *Department of Chemistry*, Doctor of Philosophy, University of Helsinki, Espoo 2006.

[3] H. M. Cheng, F. Li, G. Su, H. Pan, M. Dresselhaus, *Applied Physics Letters* 1998, *72*, 3282.

[4] P. Nikolaev, M. J. Bronikowski, R. K. Bradley, F. Rohmund, D. T. Colbert, K. A. Smith, R. E. Smalley, *Chemical Physics Letters* 1999, *313*, 91.

[5] R. Sen, A. Govindaraj, C. N. R. Rao, *Chemical Physics Letters* 1997, *267*, 276.

[6] A. Moisala, A. G. Nasibulin, D. P. Brown, H. Jiang, L. Khriachtchev, E. I. Kauppinen, *Chemical Engineering Science* 2006, *61*, 4393.

[7] A. Moisala, A. G. Nasibulin, S. D. Shandakov, H. Jiang, E. I. Kauppinen, *Carbon* 2005, *43*, 2066.

[8] A. Kaskela, A. G. Nasibulin, M. Y. Timmermans, B. Aitchison, A. Papadimitratos, Y. Tian, Z. Zhu, H. Jiang, D. P. Brown, A. Zakhidov, E. I. Kauppinen, *Nano Letters* 2010, *10*, 4349.

[9] R. Saito, G. Dresselhaus, M. S. Dresselhaus, *Physical Properties of Carbon Nanotubes*, Vol. 3, Imperial College Press, London 1998.

[10] A.Jorio, G. Dresselhaus, M. S. Dresselhaus, *Carbon nanotubes: Advanced Topics in the Synthesis, Structure, Properties and Applications*, Springer, Heidelberg 2008.

[11] R. Saito, G. Dresselhaus, M. S. Dresselhaus, *Physical Review B* 2000, *61*, 2981.

[12] Erik.Einarsson, in *Department of Mechanical Engineering*, Doctor of Philosophy, The University of Tokyo, Tokyo 2006.

[13] X. Liu, T. Pichler, M. Knupfer, M. S. Golden, J. Fink, H. Kataura, Y. Achiba, *Physical Review B* 2002, *66*, 045411.

[14] A. Jorio, C. Fantini, M. A. Pimenta, R. B. Capaz, G. G. Samsonidze, G. Dresselhaus, M. S. Dresselhaus, J. Jiang, N. Kobayashi, A. Gruneis, R. Saito, *Physical Review B* 2005, *71*, 075401.

[15] M. S. Dresselhaus, G. Dresselhaus, R. Saito, A. Jorio, *Annual Review of Physical Chemistry* 2007, *58*, 719.

[16] D. Porezag, T. Frauenheim, T. Kohler, G. Seifert, R. Kaschner, *Physical Review B* 1995, *51*, 12947.

[17] G. G. Samsonidze, R. Saito, N. Kobayashi, A. Gruneis, J. Jiang, A. Jorio, S. G. Chou, G. Dresselhaus, M. S. Dresselhaus, *Applied Physics Letters* 2004, *85*, 5703.

[18] H. Kataura, Y. Kumazawa, Y. Maniwa, I. Umezu, S. Suzuki, Y. Ohtsuka, Y. Achiba, *Synthetic Metals* 1999, *103*, 2555.

[19] S. D. M. Brown, A. Jorio, P. Corio, M. S. Dresselhaus, G. Dresselhaus, R. Saito, K. Kneipp, *Physical Review B* 2001, *63*, 155414.

[20] A. Jorio, A. G. Souza Filho, G. Dresselhaus, M. S. Dresselhaus, A. K. Swan, M. S. Unlu, B. B. Goldberg, M. A. Pimenta, J. H. Hafner, C. M. Lieber, R. Saito, *Physical Review B* 2002, *65*, 155412.

[21] M. S. Dresselhaus, G. Dresselhaus, R. Saito, A. Jorio, *Physics Reports* 2005, *409*, 47.

[22] P. T. Araujo, S. K. Doorn, S. Kilina, S. Tretiak, E. Einarsson, S. Maruyama, H. Chacham, M. A. Pimenta, A. Jorio, *Physcal Review Letters* 2007, *98*, 067401.

[23] A. G. Nasibulin, A. Moisala, D. P. Brown, H. Jiang, E. I. Kauppinen, *Chemical Physics Letters* 2005, *402*, 227.

[24] A. G. Nasibulin, P. V. Pikhitsa, H. Jiang, D. P. Brown, A. V. Krasheninnikov, A. S. Anisimov, P. Queipo, A. Moisala, D. Gonzalez, G. Lientschnig, A. Hassanien, S. D. Shandakov, G. Lolli, D. E. Resasco, M. Choi, D. Tomanek, E. I. Kauppinen, *Nature Nanotechnology* 2007, *2*, 156.

[25] C. Fantini, A. Jorio, M. Souza, M. S. Strano, M. S. Dresselhaus, M. A. Pimenta, *Physical Review Letters* 2004, *93*, 147406.

[26] M. Y. Sfeir, T. Beetz, F. Wang, L. Huang, X. M. H. Huang, M. Huang, J. Hone, S. O'Brien, J. A. Misewich, T. F. Heinz, L. Wu, Y. Zhu, L. E. Brus, *Science* 2006, *312*, 554.

[27] T. Michel, M. Paillet, J. C. Meyer, V. N. Popov, L. Henrard, J. L. Sauvajol, *Physical Review B* 2007, *75*, 155432.

[28] H. Jiang, A. G. Nasibulin, D. P. Brown, E. I. Kauppinen, *Carbon* 2007, *45*, 662.

[29] R. Pfeiffer, H. Kuzmany, T. Pichler, H. Kataura, Y. Achiba, M. Melle-Franco, F. Zerbetto, *Physical Review B* 2004, *69*, 035404.

[30] Y. Zou, B. Liu, M. Yao, Y. Hou, L. Wang, S. Yu, P. Wang, B. Li, B. Zou, T. Cui, G. Zou, T. Wågberg, B. Sundqvist, *Physical Review B* 2007, *76*, 195417.

[31] T. Pichler, H. Kuzmany, H. Kataura, Y. Achiba, *Physical Review Letters* 2001, *87*, 267401.

[32] R. Pfeiffer, H. Kuzmany, W. Plank, T. Pichler, H. Kataura, Y. Achiba, *Diamond and Related Materials* 2002, *11*, 957.

[33] P. M. Rafailov, C. Thomsen, H. Kataura, *Physical Review B* 2003, *68*, 193411.

[34] X. Liu, T. Pichler, M. Knupfer, M. S. Golden, J. Fink, H. Kataura, Y. Achiba, *Physical Review B* 2002, *66*, 045411.

[35] R. Bhowmick, B. M. Clemens, B. A. Cruden, *Carbon* 2008, *46*, 907.

[36] A. Barreiro, C. Kramberger, M. H. Rümmeli, A. Grüneis, D. Grimm, S. Hampel, T. Gemming, B. Büchner, A. Bachtold, T. Pichler, *Carbon* 2007, *45*, 55.

[37] M. Ichida, S. Mizuno, Y. Saito, H. Kataura, Y. Achiba, A. Nakamura, *Physical Review B* 2002, *65*, 241407.

[38] X. Lin, M. H. Rümmeli, T. Gemming, T. Pichler, D. Valentin, G. Ruani, C. Taliani, *Carbon* 2007, *45*, 196.

[39] J. G. Wiltshire, L.-J. Li, L. M. Herz, R. J. Nicholas, M. Glerup, J.-L. Sauvajol, A. N. Khlobystov, *Physical Review B* 2005, *72*, 205431.

[40] A. G. Ryabenko, T. V. Dorofeeva, G. I. Zvereva, *Carbon* 2004, *42*, 1523.

[41] N. Nair, M. L. Usrey, W.-J. Kim, R. D. Braatz, M. S. Strano, *Analytical Chemistry* 2006, *78*, 7689.

[42] B. J. Landi, H. J. Ruf, C. M. Evans, C. D. Cress, R. P. Raffaelle, *The Journal of Physical Chemistry B* 2005, *109*, 9952.

[43] N. P. Valentin, *New Journal of Physics* 2004, *6*, 17.

[44] C. L. Kane, E. J. Mele, *Physcal Review Letters* 2004, *93*, 197402.

[45] S. Hofmann, R. Sharma, C. Ducati, G. Du, C. Mattevi, C. Cepek, M. Cantoro, S. Pisana, A. Parvez, F. Cervantes-Sodi, A. C. Ferrari, R. Dunin-Borkowski, S. Lizzit, L. Petaccia, A. Goldoni, J. Robertson, *Nano Letters* 2007, *7*, 602.

[46] G. Lolli, L. Zhang, L. Balzano, N. Sakulchaicharoen, Y. Tan, D. E. Resasco, *The Journal of Physical Chemistry B* 2006, *110*, 2108.

[47] A. S. Anisimov, A. G. Nasibulin, H. Jiang, P. Launois, J. Cambedouzou, S. D. Shandakov, E. I. Kauppinen, *Carbon* 2010, *48*, 380.

[48] G. Dresselhaus, A. Jorio, *The Journal of Physical Chemistry C* 2007, *111*, 17887.

[49] Y. Sato, K. Yanagi, Y. Miyata, K. Suenaga, H. Kataura, S. Iijima, *Nano Lett* 2008, *8*, 3151.

[50] S. Helveg, C. Lopez-Cartes, J. Sehested, P. L. Hansen, B. S. Clausen, J. R. Rostrup-Nielsen, F. Abild-Pedersen, J. K. Norskov, *Nature* 2004, *427*, 426.

[51] P. R. Mudimela, A. G. Nasibulin, H. Jiang, T. Susi, D. Chassaing, E. I. Kauppinen, *The Journal of Physical Chemistry C* 2009, *113*, 2212.

[52] S. Kivist, T. Hakulinen, A. Kaskela, B. Aitchison, D. P. Brown, A. G. Nasibulin, E. I. Kauppinen, A. Härkönen, O. G. Okhotnikov, *Optical Express* 2009, *17*, 2358.

Aalto-DD 77/2012

ISBN 978-952-60-4659-4
ISBN 978-952-60-4660-0 (pdf)
ISSN-L 1799-4934
ISSN 1799-4934
ISSN 1799-4942 (pdf)

Aalto University
School of Science
Department of Applied Physics
www.aalto.fi

BUSINESS +
ECONOMY

ART +
DESIGN +
ARCHITECTURE

SCIENCE +
TECHNOLOGY

CROSSOVER

DOCTORAL
DISSERTATIONS